Ocean Modelling 33 (2010) 159–176

Contents lists available at ScienceDirect

Ocean Modelling

journal homepage: www.elsevier.com/locate/ocemod

A new approximation for nonlinear wave–wave interactions

William Perrie [a,b,*], Adhi Susilo [b], Bechara Toulany [a]

[a] Fisheries & Oceans Canada, Bedford Institute of Oceanography, Dartmouth, Nova Scotia, Canada
[b] Department of Engineering Mathematics and Internetworking, Dalhousie University, Halifax, Nova Scotia, Canada

ARTICLE INFO

Article history:
Received 17 June 2008
Accepted 31 December 2009
Available online 11 January 2010

Keywords:
Wind waves
Nonlinear wave–wave interactions
Quadruplets
Dominant transfer
Scaling factor
Wave spectra evolution

ABSTRACT

Modern wave models require an accurate computation of the nonlinear wave–wave interactions. This is because nonlinear wave–wave interactions play an important role in the evolution of wind waves, accounting for nonlinear transfer of wave energy to lower and higher frequencies within the spectrum. Presently, in almost all operational state-of-the-art wave models, nonlinear transfer due to wave–wave interactions are evaluated by the discrete interaction approximation (DIA), which was developed by pioneering studies led by Hasselmann more than two decades ago. Although many efforts have tried to develop new methodologies to improve DIA, its basic formulation has not changed. In this study, we present a new computational method by evaluating the dominant nonlinear wave transfer along the wavenumber and the wave directional axes, and by approximating the contributions along the resonance loci. The new method is denoted the Advanced Dominant Interaction (AvDI) method. We show that AvDI is sufficiently efficient that it can be implemented within an operational wave model. As a validation of the approach, we compare simulations of hurricane Juan with observed wave data.

Crown Copyright © 2010 Published by Elsevier Ltd. All rights reserved.

1. Introduction

In recent years, the simulation and forecasting of intense cyclones and their associated maximum waves have become important issues in coastal ocean waters, due to the increased population living in these areas and the increase in potential damage to human development and societal infrastructure. Large, complex ocean waves can be generated by marine storms and their rapidly-varying winds and they can propagate thousands of kilometers from their generation centers to coastal areas. An accurate efficient computation of nonlinear wave–wave interactions is an important key to getting reliable wave forecasts.

While numerical modeling has made impressive steps in forecasting waves on global and regional scales and considerable efforts have been made to accurately simulate and measure directional wave spectra generated by marine storms, progress in the development of operational algorithms for evaluating the nonlinear wave–wave interactions has not been as rapid. Almost all modern operational wave models implemented on large-scale lakes and oceans use the discrete interaction approximation (DIA) formulation given by Hasselmann and Hasselmann (1985) and WAMDI (1988).

This paper presents a new method to compute the nonlinear wave–wave interactions. The new method is based on the Webb–Resio–Tracy algorithm (hereafter WRT), which has been described by Webb (1978), Tracy and Resio (1982), Resio and Perrie (1991, 2008) and Van Vledder (2006). The WRT method uses scaling similarities to reduce the number of computations and thereby speed up the overall computation. We suggest that this new method is a potential candidate for further development and application in operational wave forecast models.

We start with the well-known action $N(f, \theta)$ balance equation for wind-generated waves (Komen et al., 1994). In terms of wavenumber and direction, the action density may be written as $N(k, \theta, \phi, \lambda)$ and the conservation equation is generally expressed as,

$$\frac{\partial N}{\partial t}+\frac{1}{\cos\ \phi}\frac{\partial}{\partial \phi}\dot{\phi}N\ \cos\ \theta+\frac{\partial}{\partial \lambda}\dot{\lambda}N+\frac{\partial}{\partial k}\dot{k}N+\frac{\partial}{\partial \theta}\theta_{\mathrm{g}}N=\frac{S}{\sigma} \tag{1}$$

where

$$\begin{aligned}
\dot{\phi} &= \frac{c_{\mathrm{g}}\ \cos\ \theta+U_{\phi}}{R}\\
\dot{\lambda} &= \frac{c_{\mathrm{g}}\ \sin\ \theta+U_{\lambda}}{R\ \cos\ \phi}\\
\dot{k} &= -\frac{\partial\sigma\partial d}{\partial d\partial s}-\mathbf{k}\cdot\frac{\partial \mathbf{U}}{\partial s}\\
\dot{\theta}_{\mathrm{g}} &= \dot{\theta}-\frac{c_{\mathrm{g}}\ \tan\ \phi\ \cos\ \theta}{R}\\
\dot{\theta} &= -\frac{1}{k}\left(\frac{\partial\sigma\partial d}{\partial d\partial m}-\mathbf{k}\cdot\frac{\partial \mathbf{U}}{\partial m}\right)
\end{aligned} \tag{2}$$

* Corresponding author. Address: Fisheries & Oceans Canada, Bedford Institute of Oceanography, Dartmouth, Nova Scotia, Canada. Tel.: +1 902 426 3985; fax: +1 902 426 7827.
E-mail address: parriew@dfo-mpo.gc.ca (W. Perrie).

1463-5003/$ - see front matter Crown Copyright © 2010 Published by Elsevier Ltd. All rights reserved.
doi:10.1016/j.ocemod.2009.12.009

where ϕ is latitude, λ is longitude, θ is the direction of wave propagation, s is a coordinate parallel to θ and m is a coordinate perpendicular to θ, σ is the angular frequency, R is the radius of the earth, and $U_{\phi,\lambda}$ is the ocean current component in ϕ and λ directions, respectively.

On the right side of Eq. (1), S is the net source term consisting of wind input (S_{in}), nonlinear quadruplet wave–wave interactions (S_{nl}), wave-breaking dissipation (S_{ds}) and bottom friction (S_{bot}). The nonlinear interactions (S_{nl}) are important because they distribute spectral energy to higher and lower frequencies, and directionally within the spectrum. In this paper, we focus on the nonlinear wave–wave interactions (S_{nl}), which are conservative, neither creating nor dissipating energy.

In a pioneering study, Hasselmann (1962) derived an analytic expression for S_{nl}, which is often referred to as the Boltzmann integral or kinetic equation. Some time later, Hasselmann and Hasselmann (1981) presented the Exact-NL formulation to numerically estimate S_{nl}. This method was the first systematic algorithm for this problem. However, this approach is too time-consuming for operational wave forecasting. Therefore, several years later Hasselmann et al. (1985) developed the Discrete Interaction Approximation (DIA), with dramatically increased computational efficiency compared to Exact-NL. The development of DIA allowed the formulation of third-generation wave prediction models, such as WAM, WAVEWATCHIII and SWAN. However, DIA has a number of well-known shortcomings and for many types of spectra compares poorly with a full evaluation of S_{nl} (Van Vledder, 2001; Resio and Perrie, 2008; Perrie and Resio, 2009).

In recent years, several attempts have been made to formulate a more efficient, accurate parameterization for S_{nl} by incrementally simplifying the "exact" WRT method. Lin and Perrie (1999) suggested a reduced integration approach. Several studies have tried to move beyond the basic DIA approach, expanding DIA, or using multiple representative quadruplets (Krasnopolsky et al., 2002; Tolman and Krasnopolsky, 2004; Tolman et al., 2005; Van Vledder, 2001, 2006; Tolman, 2004; Hashimoto and Kawaguchi, 2001). Recently, a two-scale approximation to wave–wave interactions has been suggested by Resio and Perrie (2008) and Perrie and Resio (2009).

Motivated by Tracy and Resio (1982), Susilo and Perrie (2007) developed an algorithm that estimates a scaling factor to evaluate the nonlinear transfer, based on the largest contributions, or dominant contributions, to S_{nl} along the mean wave direction. This method achieves a reduction in computational time by selecting sets of interacting wavenumbers that produce the dominant transfers so that it is not necessary to compute the integral for the entire spectrum. However, the method needs additional optimization before it can be applied for operational forecast models.

In this study, a modern operational third-generation spectral wave model is used to test the new AvDI formulation for nonlinear wave–wave interactions, WAVEWATCH III (hereafter WW3) version 1.18 (Tolman, 1999, 2002). WW3 includes numerical and physical parameterizations that make it suitable for a large range of scales including global, ocean-basin scale, shelf scales, and high-resolution coastal ocean regions. We first present a theoretical development of the AvDI method in Section 2, based on the WRT methodology. As a practical demonstration, AvDI is implemented in WW3 in Section 3. Results from numerical experiments, involving both JONSWAP wave observations and a real storm case are described in Section 4. Tests involving storm-generated waves are important because parameterizations for S_{nl} have sometimes been found to perform much better for JONSWAP spectra than for evolutionary storm cases (Tolman, 2004). In this study, the storm is hurricane Juan which made landfall in Halifax, Nova Scotia on September 29, 2003 as a category two hurricane. Model validation is based on wave buoy observations. Conclusions are given in Section 5.

2. Theoretical and numerical development

The basic equation describing the nonlinear quadruplet wave–wave interactions (Hasselmann, 1962; Zakharov and Filonenko, 1966) is known as the full Boltzmann integral (FBI). This relation gives the rate of change of action density S_{nl}, due to all resonant interactions among quadruplets of wave numbers. It may be expressed as

$$\frac{\mathrm{d}N_1}{\mathrm{d}t} = \int\int\int C^2(\mathbf{k}_1,\mathbf{k}_2,\mathbf{k}_3,\mathbf{k}_4)D(\mathbf{k}_1,\mathbf{k}_2,\mathbf{k}_3,\mathbf{k}_4) \times \delta(\mathbf{k}_1+\mathbf{k}_2-\mathbf{k}_3-\mathbf{k}_4)\delta(\omega_1+\omega_2-\omega_3-\omega_4)\mathrm{d}\mathbf{k}_2\mathrm{d}\mathbf{k}_3\mathrm{d}\mathbf{k}_4 \quad (3)$$

where

$$D(\mathbf{k}_1,\mathbf{k}_2,\mathbf{k}_3,\mathbf{k}_4) = N_1N_3(N_4-N_2)+N_2N_4(N_3-N_1) \quad (4)$$

and where N_1 is the action density at wave number $\mathbf{k}_1$. Webb (1978) expressed this equation in terms of a transfer function $T(\mathbf{k}_1,\mathbf{k}_3)$ where

$$\frac{\mathrm{d}N_1}{\mathrm{d}t} = 2\int T(\mathbf{k}_1,\mathbf{k}_3)d\mathbf{k}_3 = 2\int_0^\infty\int_0^{2\pi} T(\mathbf{k}_1,\mathbf{k}_3)\ \mathbf{k}_3\mathrm{d}\theta_3\mathrm{d}\mathbf{k}_3 \quad (5)$$

and

$$T(\mathbf{k}_1,\mathbf{k}_3) = \int\int C^2(\mathbf{k}_1,\mathbf{k}_2,\mathbf{k}_3,\mathbf{k}_4)D(\mathbf{k}_1,\mathbf{k}_2,\mathbf{k}_3,\mathbf{k}_4) \times \delta(\mathbf{k}_1+\mathbf{k}_2-\mathbf{k}_3-\mathbf{k}_4)\delta(\omega_1+\omega_2-\omega_3-\omega_4) \times \Theta(|\mathbf{k}_1-\mathbf{k}_4|-|\mathbf{k}_1-\mathbf{k}_3|)\mathrm{d}\mathbf{k}_2\mathrm{d}\mathbf{k}_4. \quad (6)$$

Here, ω_i is the angular frequency at $\mathbf{k}_i$, $\delta(\ldots)$ is the Dirac delta function, C^2 is the coupling coefficient (Webb, 1978; Tracy and Resio, 1982) and Θ is the Heaviside function,

$$\Theta(x) = 1 \quad \text{if} \quad x > 0$$
$$\Theta(x) = 1 \quad \text{if} \quad x \leqslant 0$$
$$x = |\mathbf{k}_1-\mathbf{k}_4|-|\mathbf{k}_1-\mathbf{k}_3|. \quad (7)$$

Applying the resonance conditions $\omega_1+\omega_2=\omega_3+\omega_4$ and $\mathbf{k}_1+\mathbf{k}_2=\mathbf{k}_3+\mathbf{k}_4$, Tracy and Resio (1982) and Resio and Perrie (1991) restated the transfer integral (Eq. (6)) as

$$T(\mathbf{k}_1,\mathbf{k}_3) = \int_C C^2D\left|\frac{\partial W}{\partial \mathbf{n}}\right|^{-1}\Theta(\mathbf{k}_1,\mathbf{k}_3,\mathbf{k}_4)\mathrm{d}\mathbf{s} \quad (8)$$

which is a contour integral. Here, $W=\omega_1+\omega_2+\omega_3+\omega_4$, the frequency resonance condition is $W=0$, unit vector $\mathbf{s}$ is along the interaction locus, and unit vector $\mathbf{n}$ is normal to that locus. In terms of a density function $D(N)$ and a geometry function $G(\mathbf{k})$, Eq. (8) may be written as

$$T(\mathbf{k}_1,\mathbf{k}_3) = \int_C D(N)G(\mathbf{k}) \quad (9)$$

where

$$G(k) = C^2\left|\frac{\partial W}{\partial n}\right|^{-1}\Theta(\mathbf{k}_1,\mathbf{k}_3,\mathbf{k}_4)\mathrm{d}\mathbf{s}. \quad (10)$$

In evaluating the full Boltzmann integral, Eq. (5) may be expressed as

$$\frac{\mathrm{d}N_1}{\mathrm{d}t} = \int_0^\infty\int_0^{2\pi}\int_C \ldots\ \mathrm{d}\mathbf{s}\mathrm{d}\theta_3\mathrm{d}\mathbf{k}_3 \quad (11)$$

where it is important to include all contributions from the entire domain of the wave spectra including all possible resonance combinations satisfying the interaction loci. If there are i frequency bins, j angle bins and l loci bins, the integral requires $i\times j\times l$ calculations to compute $\mathrm{d}N_1/\mathrm{d}t$, compared to DIA which requires $i\times j$

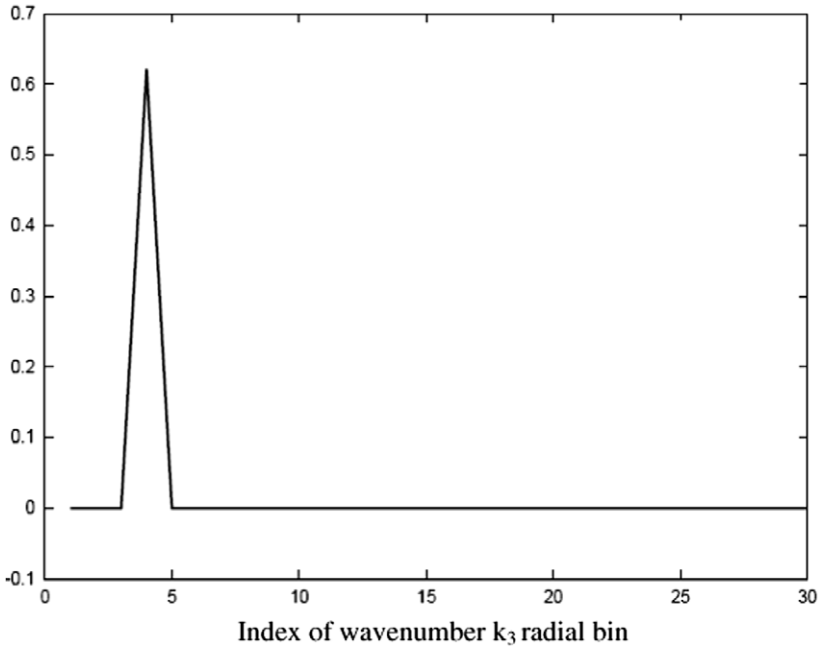

Fig. 1. Example of dominant transfer along the wave number axis. The *y*-axis gives the 1-dimensional contributions to the integrand in Eq. (5), with θ already integrated from 0 to 2π; the *x*-axis is the wavenumber k_3 radial index, extending over all wavenumber bins. The index of the k_1 wavenumber bin is 5 in Eq. (5).

calculations for the same grid. These constraints make the FBI formulation very time-consuming.

Tracy and Resio (1982) and Resio and Perrie (1991) used a polar coordinate system with radial coordinates logarithmically spaced according to

$$\mathbf{k}_{m+1} = \lambda \mathbf{k}_m \tag{12}$$

where $m+1$ is the radial coordinate index. Therefore, for any geometrically similar $\mathbf{k}_1$ and $\mathbf{k}_3$, such as $|\mathbf{k}_1' - \mathbf{k}_3'| = \lambda|\mathbf{k}_1 - \mathbf{k}_3|$, the locus equation also scales linearly. Specifically, for each point along the original locus there is a geometrically similar point on a scaling locus such that $\mathbf{k}_2' = \lambda \mathbf{k}_2$. The resonance conditions imply that $\mathbf{k}_4' = \lambda \mathbf{k}_4$, and for each combination of wavenumbers satisfying $(\mathbf{k}_1', \mathbf{k}_2', \mathbf{k}_3', \mathbf{k}_4') = \lambda(\mathbf{k}_1, \mathbf{k}_2, \mathbf{k}_3, \mathbf{k}_4)$ it follows that

$$C^2(\mathbf{k}_1', \mathbf{k}_2', \mathbf{k}_3', \mathbf{k}_4') = \lambda^6 C^2(\mathbf{k}_1, \mathbf{k}_2, \mathbf{k}_3, \mathbf{k}_4) \tag{13}$$

$$|\partial W'/\partial n|^{-1} = \lambda^{1/2} |\partial W/\partial n|^{-1} \tag{14}$$

$$\mathbf{d}s' = \lambda \mathbf{d}s. \tag{15}$$

Therefore, using m_i as the radial index of the polar coordinate grid, and n_i as the angular index for the ith wavenumber, then C^2, $|\partial W/\partial \mathbf{n}|^{-1}$ and d*s* need to be calculated only once for each different $m_3 - m_1$ and $n_3 - n_1$. Letting $\mathbf{k}_1 = (\mathbf{k}_0, 0)$ and $\mathbf{k}_3$ vary over the entire grid, we initially construct a table of values for $C^2|\partial W/\partial \mathbf{n}|^{-1}\,\mathbf{d}s$. All other locus solutions, coupling coefficients, Jacobian terms and phase space volumes can be obtained by appropriate multiplication of these results. For example, if $|\mathbf{k}_1' - \mathbf{k}_3'| = \lambda^j |\mathbf{k}_1 - \mathbf{k}_3|$ then it follows that

$$C^2(\mathbf{k}_1', \mathbf{k}_2', \mathbf{k}_3', \mathbf{k}_4')|\partial W/\partial \mathbf{n}|^{-1}\mathbf{d}\mathbf{s} = (\lambda)^{15j/2} C^2(\mathbf{k}_1, \mathbf{k}_2, \mathbf{k}_3, \mathbf{k}_4)|\partial W/\partial \mathbf{n}|^{-1}\mathbf{d}\mathbf{s}. \tag{16}$$

With the computation of $D(N)$ and the integration around the locus *s*, evaluation of the transfer integral (Eq. (8)) is complete. Thus, integration over all $\mathbf{k}_3$ values gives the rate of change of action density, N_1 in Eqs. (3) and (5). With this approach, the basic geometry function $G(\mathbf{k})_{\text{basic}}$ needs to be calculated only once. Related calculations for other $G(\mathbf{k})$s are then inferred as $G(\mathbf{k})_{\text{next}} = G(\mathbf{k})_{\text{basic}} \times \lambda^{15j/2}$, where $\lambda^{15j/2}$ is the scale factor.

Based on this formulation, Susilo and Perrie (2007) developed a preliminary methodology which they denoted the *dominant transfer approximation* (or DTA) to reduce the number of loops of the integration. They found a set of coordinates $(\mathbf{k}_1, \mathbf{k}_3)$ which gives the maximum transfer, as illustrated in Fig. 1. In particular, Fig. 1 gives the 1-dimensional contributions to the integrand in Eq. (5), where the *x*-axis is the wavenumber radial $\mathbf{k}_3$ index, extending over all the wavenumber bins, and θ has already been integrated from 0 to 2π. In Fig. 1, we let $\mathbf{k}_1$ have index 5 (see Eq. (5)), as discussed in Fig. 1a in Susilo and Perrie (2007). In the latter study, additional cases are also considered, where the index of $\mathbf{k}_1$ is 10, 15 and 30.

The DTA formulation selects the $(\mathbf{k}_1, \mathbf{k}_3)$ coordinates and then uses a multiplicative scaling factor to approximate the integral over the entire 2-dimensional spectrum. With this method, Eq. (11) can be rewritten as

$$\frac{\mathrm{d}N_1}{\mathrm{d}t} \approx F_{\mathrm{d}} \int_0^{2\pi} \int_C \ldots\ldots\ \mathrm{d}s\mathrm{d}\theta_3 \tag{17}$$

or

$$\frac{\mathrm{d}N_1}{\mathrm{d}t} \approx F_{\mathrm{d}} \int_0^{2\pi} T(\mathbf{k}_1, \mathbf{k}_{3_{\mathrm{d}}}) \Delta \mathbf{k}_{3_{\mathrm{d}}} \mathbf{k}_{3_{\mathrm{d}}} \mathrm{d}\theta_3 \tag{18}$$

where F_{d} is a multiplicative scaling factor, which we denote as the dominant factor, and $(\mathbf{k}_1, \mathbf{k}_{3_{\mathrm{d}}})$ is the set of coordinates where the maximum transfer occurs.

To improve the DTA method, we found that the maximum transfer also occurs at certain spreading angles, as shown in Fig. 2. To differentiate this method from the previous methodology, we denote this as the *advanced dominant interaction* (AvDI) method. The AvDI approach will be shown to achieve a more efficient computation, compared to previous formulations considered in this paper. To further increase the computation efficiency along the resonant loci, the Newton–Cotes method (Krommer and Ueberhuber, 1994) is used, implementing a 10-point approximation formula (Ueberhuber, 1997), as described in Appendix A. The resulting dominant transfer along frequency and angle coordinates can be simplified to

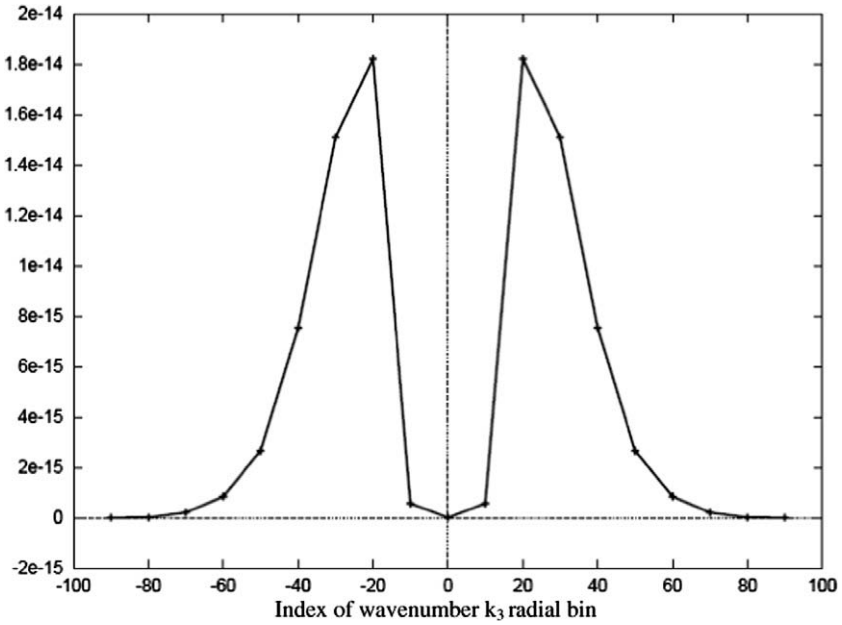

Fig. 2. As in Fig. 1, as an example of dominant transfer with respect to angle. The *y*-axis gives the 1-dimensional contributions to the integrand in Eq. (5), with the radial k_3 integrated over its domain; the *x*-axis is the wavenumber k_3 angular index, extending over all angular bins.

$$\frac{dN_1}{dt} \approx F_d \sum_{\theta_1}^{\theta_2} \int_1^{18} \dots ds \tag{19}$$

or

$$\frac{dN_1}{dt} \approx F_d [T(\mathbf{k}_1, \mathbf{k}_{3_{d(-)}}) \Delta \mathbf{k}_{3_d} \mathbf{k}_{3_d} \Delta\theta_3 + T(\mathbf{k}_1, \mathbf{k}_{3_{d(+)}}) \Delta \mathbf{k}_{3_d} \mathbf{k}_{3_d} \Delta\theta_3] \tag{20}$$

where

$$\mathbf{k}_{3d(-)} = \left(\mathbf{k}_{3d}, \theta_{\mathbf{k}_1} - \frac{1}{9}\pi\right) \tag{21}$$

$$\mathbf{k}_{3d(+)} = \left(\mathbf{k}_{3d}, \theta_{\mathbf{k}_1} + \frac{1}{9}\pi\right) \tag{22}$$

Therefore, computing the nonlinear transfer in ($\mathbf{k}_i$, $\mathbf{k}_j$) wavenumber space with $\mathbf{k}_l$ points on the locus requires only $i \times j \times 1 \times 2 \times 18$ computations rather than $i^2 \times j^2 \times l$, because the 10-point approximation has nine sub-sections; thus 18 computations are needed on the locus.

3. Wave model description

In this section we describe the implementation of AvDI in WW3, hereafter denoted WW3-AvDI. WW3 uses an explicit scheme to solve the action balance (Eq. (1)) for *N* and allows a variety of different source term formulations for wind input (S_{in}) and wave-breaking dissipation (S_{ds}). The default set-up corresponds to the wave-boundary layer formulation for S_{in} and S_{ds} due to Tolman and Chalikov (1996). Tolman (2002) notes that application of this formulation, as with any parameterizations for S_{in} and S_{ds}, has entailed a correction in fetch-limited wave heights that results from atmospheric stratification. This correction necessitates a re-tuning of the model by defining 'effective' winds, as well as an additional correction for the impact of stability on wave-growth. An alternate combination for S_{in} and S_{ds} corresponds to WAM cycle 3 physics, as described by WAMDI (1988) and Komen et al. (1994). In this paper, we essentially use the default versions for S_{in} and S_{ds}, due to Tolman and Chalikov (1996), which are shown by Padilla-Hernández et al. (2007) to be competitive, compared to the WAM cycle 3 formulations for S_{in} and S_{ds}, in tests with Northwest Atlantic storm-generated waves. In typical operational forecasts using a model such as WW3, the nonlinear interactions S_{nl} are simulated by DIA. Implementation of a new S_{nl} parameterization can involve an extensive program to re-tune of the other source terms (S_{in} and S_{ds}) in order to achieve optimal simulations of wave-growth relations, with respect to fetch and duration, compared to storm-generated wave observations. However, extensive tuning of S_{in} and S_{ds} is beyond the scope of this manuscript, and is being pursued in related studies. The integration scheme used in WW3 is the Ultimate Quickest (UQ) propagation scheme with diffusion, in the case of either DIA or AvDI. UQ is semi-implicit and third-order accurate in both space and time.

This section is divided into two parts. The first part will discuss the model set-up for tests using JONSWAP (Hasselmann et al., 1973) spectral cases. The second part describes modifications needed to install AvDI into WW3 for tests with wave data collected during hurricane Juan.

3.1. Model set-up for JONSWAP tests

The AvDI formulation assumes the polar coordinate grid of Tracy and Resio (1982), whereby the coupling coefficient and Jacobian in Eq (7) are fixed along the interaction resonance loci. As this grid is quite similar to the basic WW3 grid, we also take this approach for the model set-up for JONSWAP test cases and for the hurricane Juan case. Details regarding the spectral range and resolution of the three models are given in Table 1, in terms of the lowest and highest wavenumbers (k_{low} and k_{high}), number of wavenumber bins (i), wavenumber resolution (Δk) and angular resolution ($\Delta\theta$). The incremental factor for the associated frequency grid is 1.1 and

Table 1
Spectral domain for the wave model.

Parameters	Values
k_{low}, k_{high} (m^{-1})	0.0068, 0.6630
i_k, Δk	30, $(\lambda - 1)$k
j_θ, $\Delta\theta$	18, 10°
Loci points	36

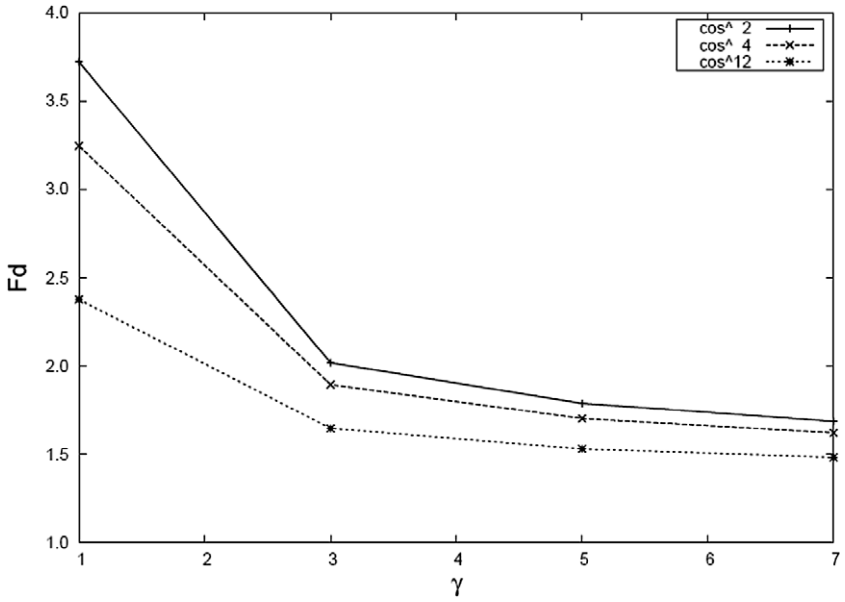

Fig. 3. F_d as a function of γ and *spreading factor*.

the resolution for the angular spreading and resonant loci is 10°. For JONSWAP tests, we use only a half-circle to represent the directional bins, with an angular domain extending from −90° to +90°.

If we assume there are 36 points on the resonant loci, the WRT formulation will need $30 \times 18 \times 30 \times 18 \times 36 = 10{,}497{,}600$ calculations, whereas the AvDI formulation will need only $30 \times 18 \times 1 \times 2 \times 18 = 19{,}440$ calculations. While WRT uses all wavenumbers, all angles and all points on the resonance loci for the interacting wavevectors, DTA is a reduction in this effort because only one frequency bin is needed for one of the wavenumbers. By comparison, AvDI represents a further reduction in effort, because it only uses one frequency bin, two angular bins, and 18 resonance bins.

In particular, two angular bins result from taking the average of the locations of the maximum transfer along the direction axis, as stated in Eqs (21) and (22) and as depicted in Fig. 2. The integral along the resonant loci is approximated by the 2×10-point trapezoidal rule. Susilo and Perrie (2007) showed that F_d is a function of peakedness (γ) and the spectral spreading, as shown in Fig. 3. Susilo et al. (2007) developed an experimental numerical fuzzy logic method to determine the F_d term, which we also implement in the AvDI formulation to compute the scaling factor F_d.

Why does F_d vary the way that it does? From Fig. 3, it follows that as γ increases, F_d decreases. This occurs because the S_{nl} peaks become sharper as γ increases, and thus become more representative of the dominant nonlinear transfer. Therefore, the multiplicative F_d factor does not need to be as large as when γ is smaller, for example ~1 or 2, and when S_{nl} peaks are smaller in magnitude. Similarly, as exponent n in the assumed spectral spreading $2\pi^{-1}\cos^{2n}\theta$ (used in training AvDI) becomes larger, F_d also decreases. This again occurs because the S_{nl} peaks become sharper as n increases, whether they are maxima or minima, and thus become more representative of the dominant transfer, and the multiplicative F_d factor does not need to be as large as when n is smaller, for example ~2 or 4, and when the S_{nl} peaks are not as large in magnitude.

3.2. Model set-up for real storm spectra

A different angular computational domain is used for wave model simulations of hurricane Juan, compared to what is needed for JONSWAP tests. The JONSWAP tests used in Section 3.1 only consider integration over a half-circle, from −90° to +90° because the wave spectra are simple, symmetric distributions generated by constant offshore winds oriented perpendicular to the coastline. By comparison, the waves generated by hurricane Juan are driven by winds that are rapidly changing in direction as the storm propagates from the open ocean to landfall. Therefore, WW3 needs to be able to simulate the waves over a 360° directional domain. For the hurricane Juan tests, AvDI must be adjusted before it can be installed into WW3. A correction to F_d is needed in order to accommodate WW3 over the 360° domain. From numerical experiments, it is found that $F_d(360°) = 0.375 \times F_d(180°)$.

4. Results

In this section, we present wave estimates using WW3 and the AvDI formulation for the nonlinear transfer S_{nl}. Tests include JONSWAP spectra cases and growth curve relations, as well as observed storm wave spectra from hurricane Juan.

4.1. Experimental cases

Using JONSWAP test spectra, we compare S_{nl} estimates from the new AvDI formulation, to our previous DTA formulation, the highly accurate WRT method, and the operational DIA. The model set-up follows the description in Section 3 and Table 1. In these simulations, we assume the JONSWAP spectral parameters have the following values: Phillips α coefficient is 0.01, peak spectral width parameters $\sigma_a = 0.07$ and $\sigma_b = 0.09$, peak frequency $f_p = 0.3$ Hz, peakedness $\gamma = 1, 3, 5, 7$, and spreading distribution is $2\pi^{-1}\cos^2\theta$. One-dimensional results for the four S_{nl} formulations are shown in Fig. 4a–d, two-dimensional results for WRT, AvDI and DIA are given in Figs. 5–8, estimates of computational run times are given in Table 2, and comparisons with JONSWAP growth curve relations are presented in Fig. 9a and b.

The one-dimensional comparisons in Fig. 4a–d suggest that AvDI generally compares well with WRT, particularly for the low frequency positive lobe. Some discrepancies are apparent in the higher frequency region of the spectrum, for the negative lobe of the nonlinear transfer, and for higher γ values. Results for AvDI are similar to those of DTA in all cases, reflecting the methodology that was applied in both formulations. On the other hand, DIA

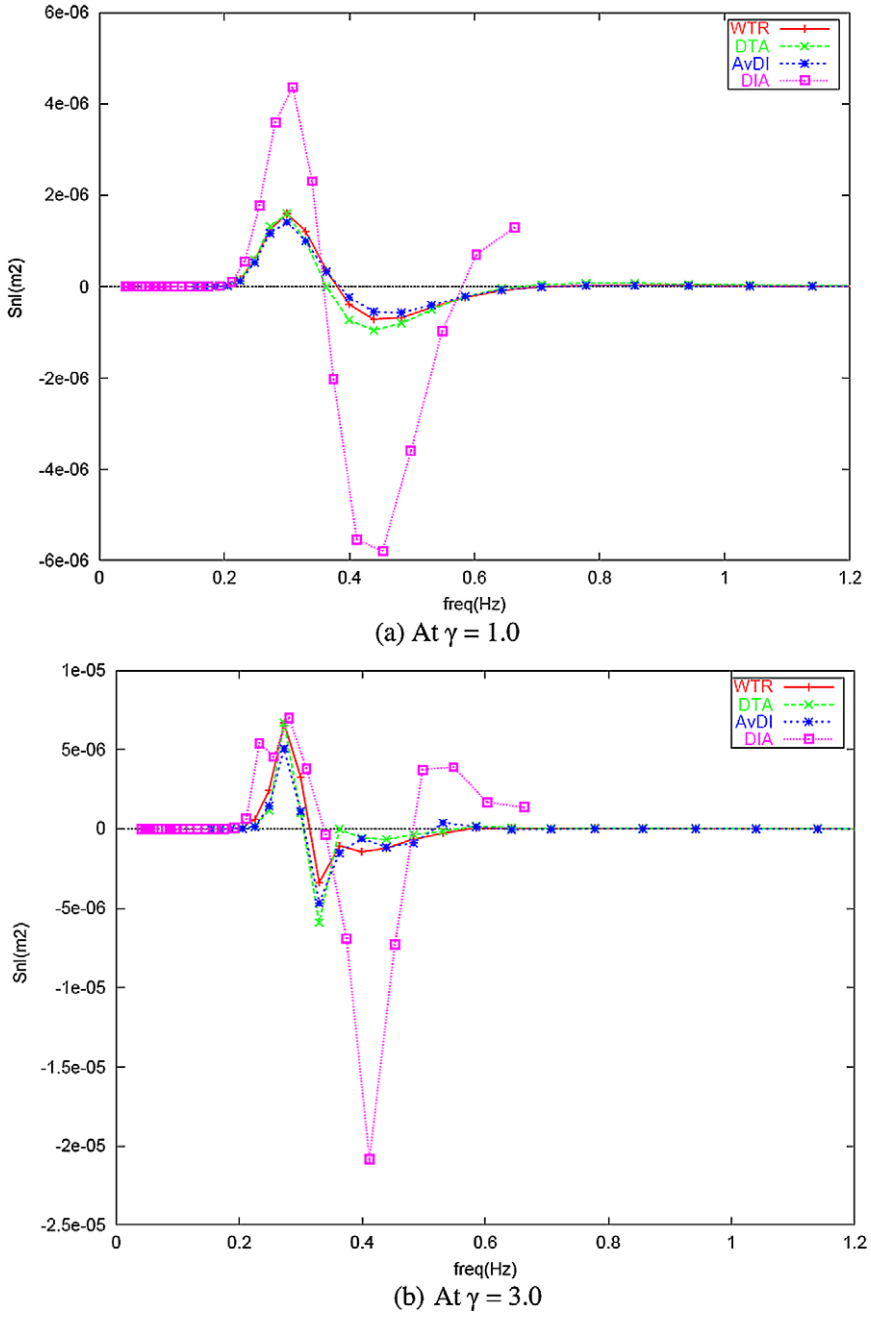

Fig. 4. One-dimensional S_{nl} comparisons for JONSWAP spectrum cases with peakedness γ values of (a) 1.0, (b) 3.0, (c) 5.0 and (d) 7.0.

results are clearly different from AvDI or WRT results in all regions of the spectrum.

Fig. 4a suggests that although DIA has the same basic pattern as the other two formulations, DIA tends to overestimate the transfer in the spectral forward face ($f/f_p < 1.0$), the spectral rear face ($1 < f/f_p < 1.5$), and for higher frequencies within the equilibrium range ($1.5 < f/f_p < 3.0$). At peakedness $\gamma = 3.0$ (Fig. 4b), the negative DIA lobe has much greater magnitude than the positive lobe, or the corresponding estimates from WRT or AvDI. Moreover, DIA also suggests that positive transfer occurs at higher frequencies, and that it has larger values than the transfer suggested by either WRT or AvDI. At $\gamma = 5.0$ (Fig. 4c), DIA suggests two positive peaks on the forward face. At higher frequencies and in the rear face region, DIA suggests excessive negative transfer compared to results for WRT or AvDI. In the high frequency equilibrium range region, DIA suggests positive transfer which is quite large, compared to WRT or AvDI results. For $\gamma = 7.0$, Fig. 4d shows similar trends, although DIA is clearly quite complicated compared to AvDI or WRT, with two positive peaks at low frequencies and excessive positive transfer at high frequencies. DIA's maximum positive transfer is shifted to lower frequencies on the spectral forward face, compared to the locations of maximum positive transfer values for WRT or AvDI. On the spectral rear face, DIA suggests two negative transfer peaks with a minimum that exceeds those of WRT or AvDI.

Figs. 5–8 show two-dimensional results, comparing S_{nl} estimates from WRT, AvDI and DIA, for peakedness γ values used in Fig. 4a–d. These results suggest that AvDI results are quite similar to those of WRT, whereas DIA estimates are very different. In particular, contours depicting the positive and negative lobes of AvDI's results near the spectral peak are very similar to those of WRT. In

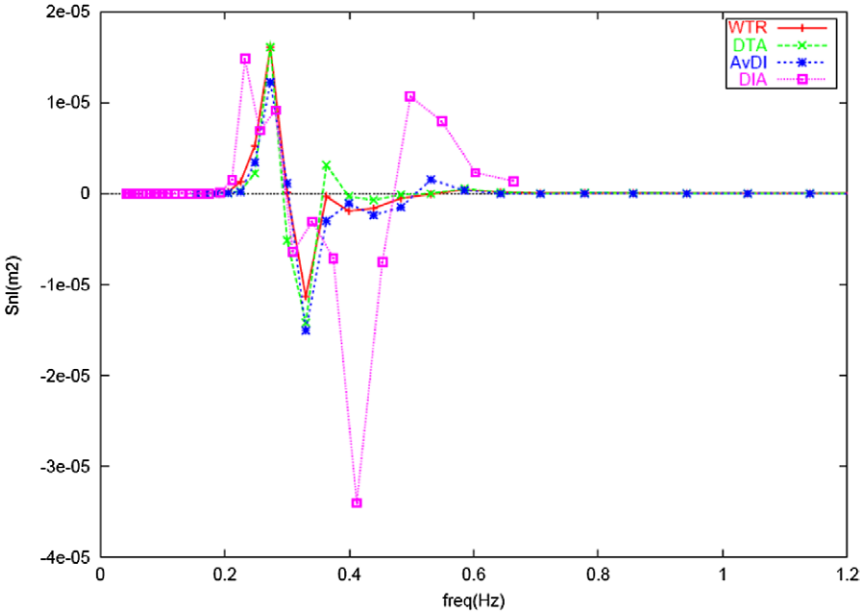

(c) At $\gamma = 5.0$.

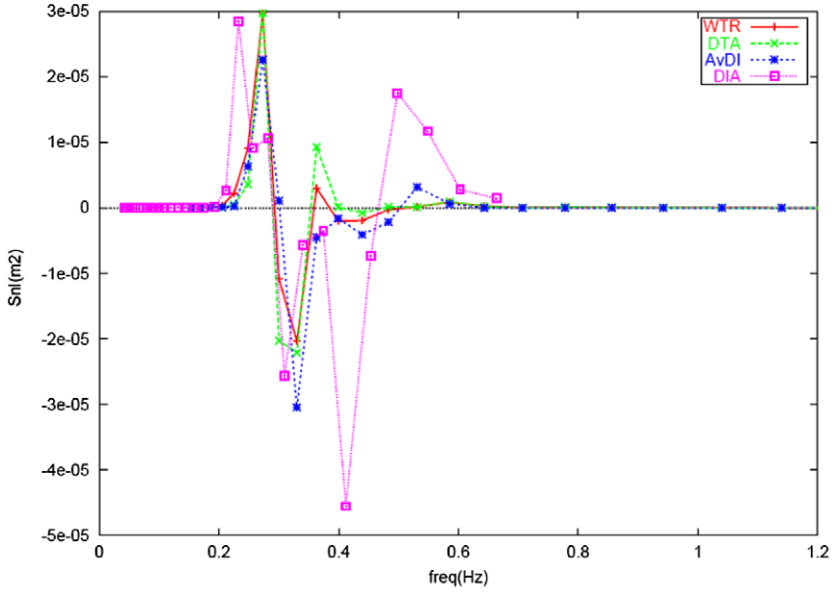

(d) At $\gamma = 7.0$.

Fig. 4 (*continued*)

AvDI's results, the positive lobes in the high frequency equilibrium range are too high, compared to WRT results, especially at high γ values. Results from DIA, as presented in Figs. 5–8 differ from WRT or AvDI, in both magnitude and contour shape.

At $\gamma = 1.0$ (Fig. 5c), DIA has wider directional contours than either WRT or AvDI. With increasing γ, the differences between DIA, WRT and AvDI become more accentuated. At $\gamma = 3.0$ (Fig. 6c), DIA suggests that the negative nonlinear transfer on the spectral rear face is much more dominant than the positive lobe on the spectral forward face. Two positive transfer peaks appear in the high frequency equilibrium range of the spectrum. At $\gamma = 5.0$ (Fig. 7c), DIA gives four minor positive peaks on the spectral forward face, two major negative peaks on the rear face and two additional positive peaks in the equilibrium range, displaying a pattern that is markedly different from WRT or AvDI patterns. This behaviour is accentuated when $\gamma = 7.0$ in Fig. 8c, where DIA suggests that the maximum positive lobe shifts to lower frequency values on the forward face, compared to results from WRT or AvDI. Negative DIA peaks on the rear face are more pronounced than results obtained for $\gamma = 5.0$ (Fig. 7c), as are two positive transfer peaks (in Fig. 8c) in the spectral equilibrium range.

Results shown in Figs. 4–8 for 1d and 2d directional transfer rates (S_{nl}) for cases with peakedness $\gamma = 1, 3, 5, 7$ are used to train the model. Additional cases such as $\gamma = 2, 4, 6$ are actual test cases, and essentially give the same results as presented in Susilo et al. (2007) and will not be repeated here. These results show that the agreement between AvDI and WTR is good. By comparison, DIA exhibits maxima and minima peaks that exceed corresponding results from WRT or AvDI, and that occur in different locations in the direction and frequency coordinates. In relative terms, the accuracy of AvDI is similar to that shown by Tolman (2004) in his test case using $\gamma = 2$ (his Fig. 2d).

Table 2 gives the relative computational time requirements for these different formulations for S_{nl} for one time-step simulations

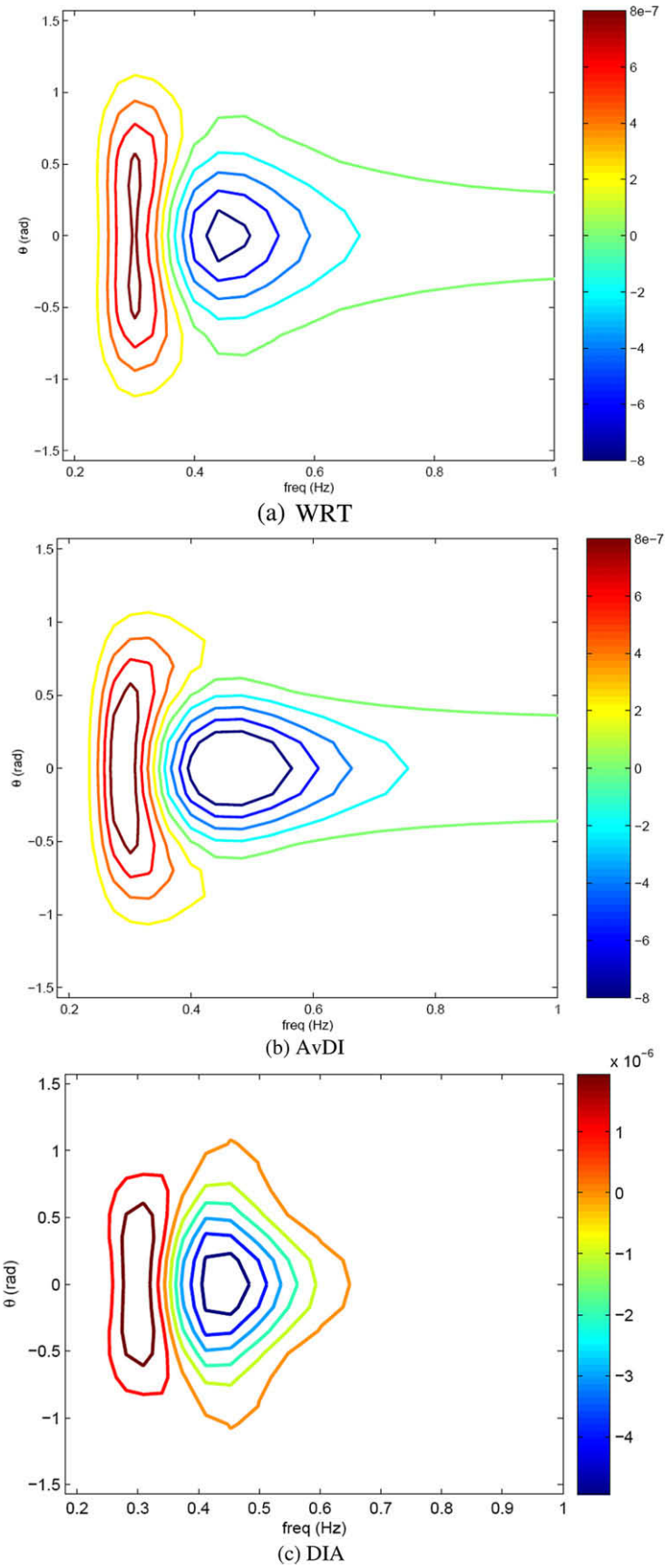

Fig. 5. Two-dimensional S_{nl} comparisons for JONSWAP spectrum cases with peakedness $\gamma = 1.0$, for (a) WRT, (b) AvDI and (c) DIA.

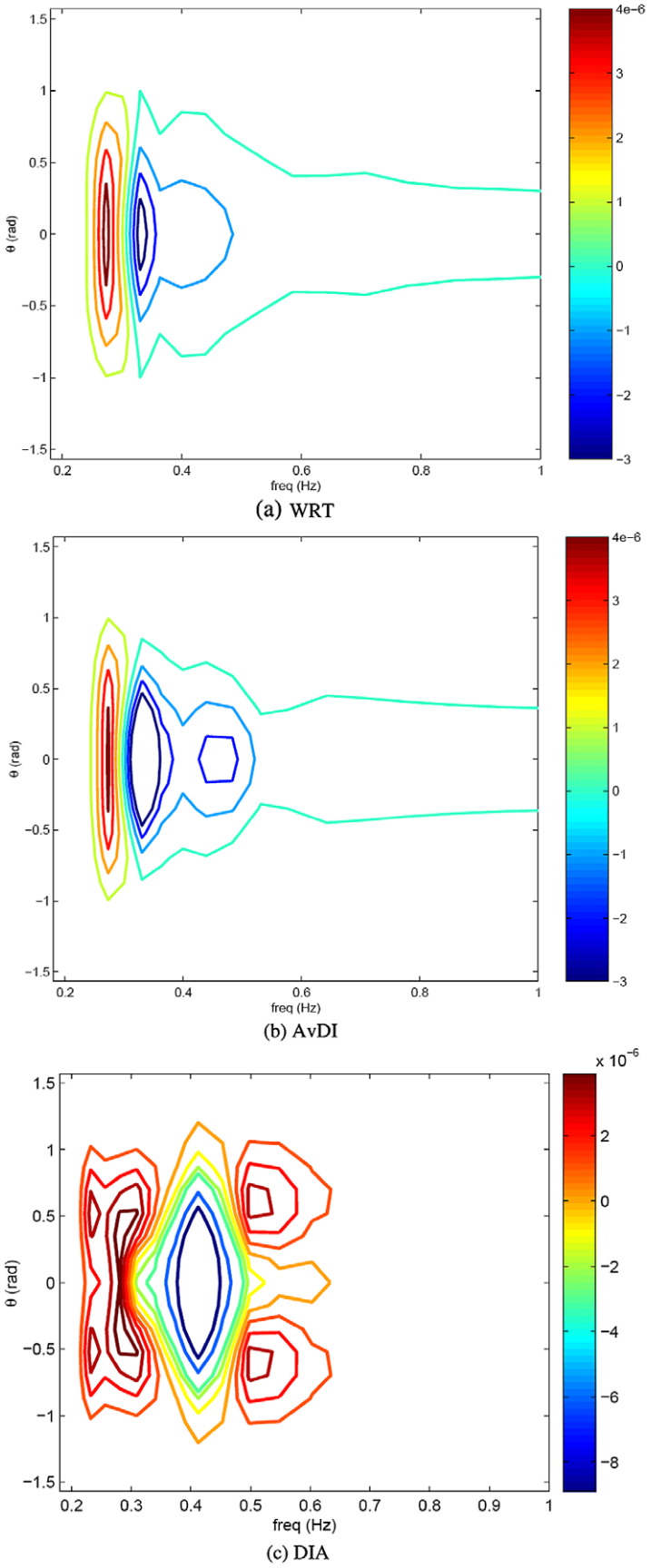

Fig. 6. As in Fig. 5, two-dimensional S_{nl} comparisons for JONSWAP spectrum cases with peakedness $\gamma = 3.0$.

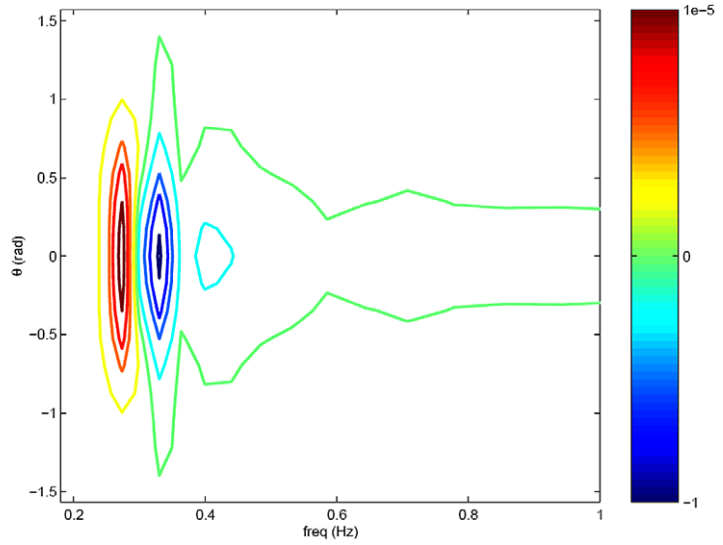

(a) WRT

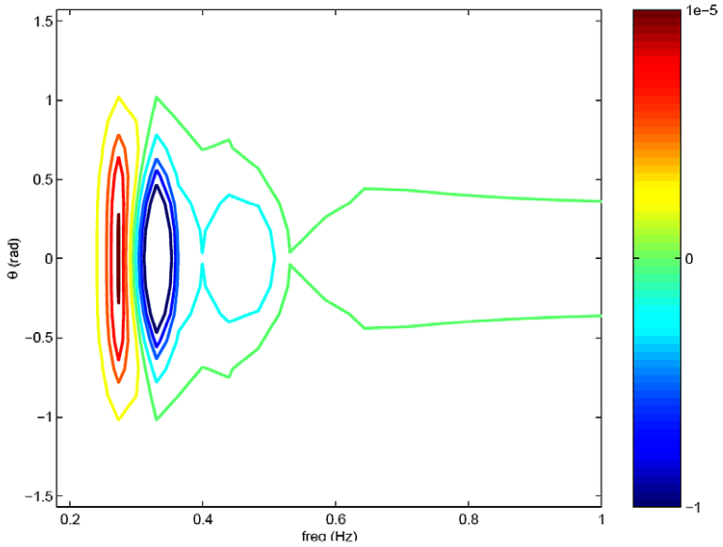

(b) AvDI

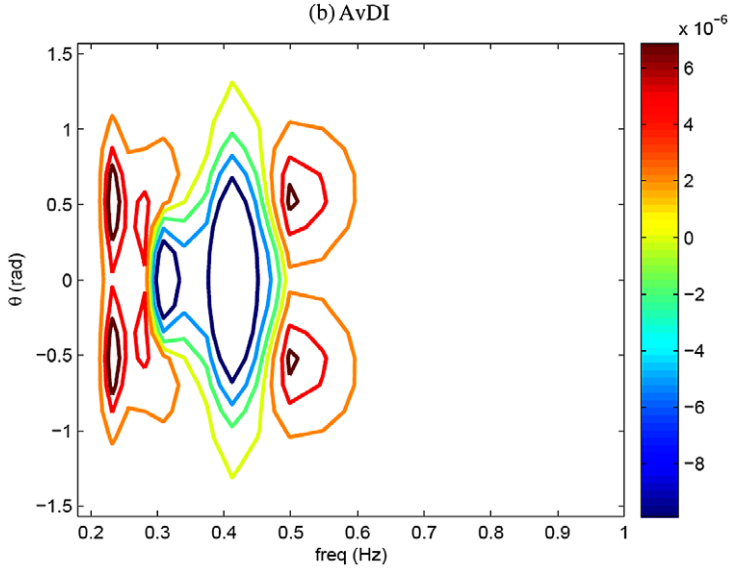

(c) DIA

Fig. 7. As in Fig. 5, two-dimensional S_{nl} comparisons for JONSWAP spectrum cases with peakedness $\gamma = 5.0$.

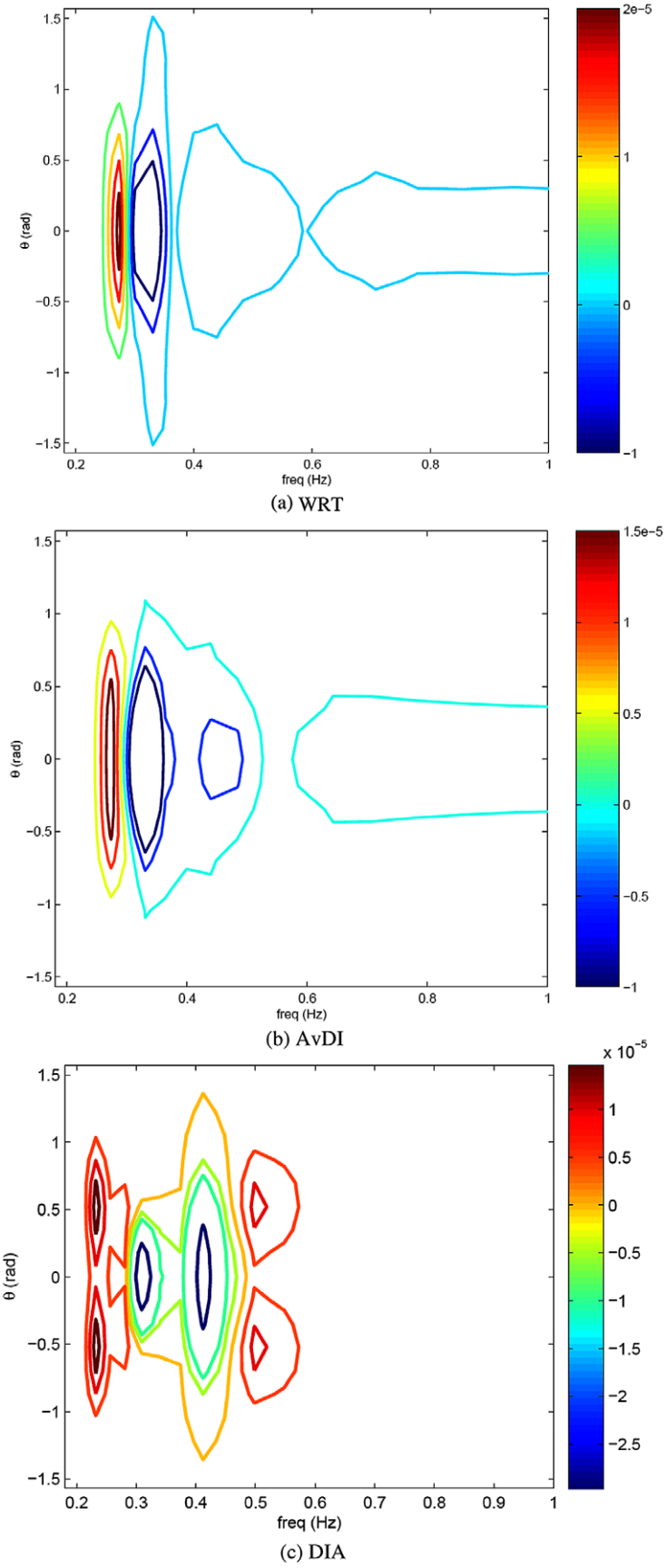

Fig. 8. As in Fig. 5, two -dimensional S_{nl} comparisons for JONSWAP spectrum cases with peakedness $\gamma = 7.0$.

Table 2
Relative computational time for S_{nl4} formulations for $30 \times 18 \times 36$ grid.

Method	Time compared to DIA
Exact	12,163
WRT	4864
DTA	633
AvDI	36
DIA	1

on a reference $30 \times 18 \times 36$ grid. These results suggest that although AvDI is much faster than either Exact-NL or WRT formulations, it is still about 36 times slower than DIA. For the time constraints and requirements of operational wave forecasts, this may not be competitive with DIA. In this comparison, Exact-NL is the formulation of Hasselmann and Hasselmann (1981) without the scaling geometry described in Section 2, as implemented in WRT. Thus, its computation time is relatively slow compared to WRT, because although both methods use the same frequency and angle domain, Exact-NL explicitly does all the computations, without taking advantage of the scaling that is possible.

Fig. 9a and b present the growth curves for WW3-AvDI, WW3-WRT and WW3-DIA for total dimensionless energy as functions of dimensionless fetch and time. Total dimensionless spectral energy is computed by integrating the spectral energy over the direction and frequency domain to get the total spectral wave energy E

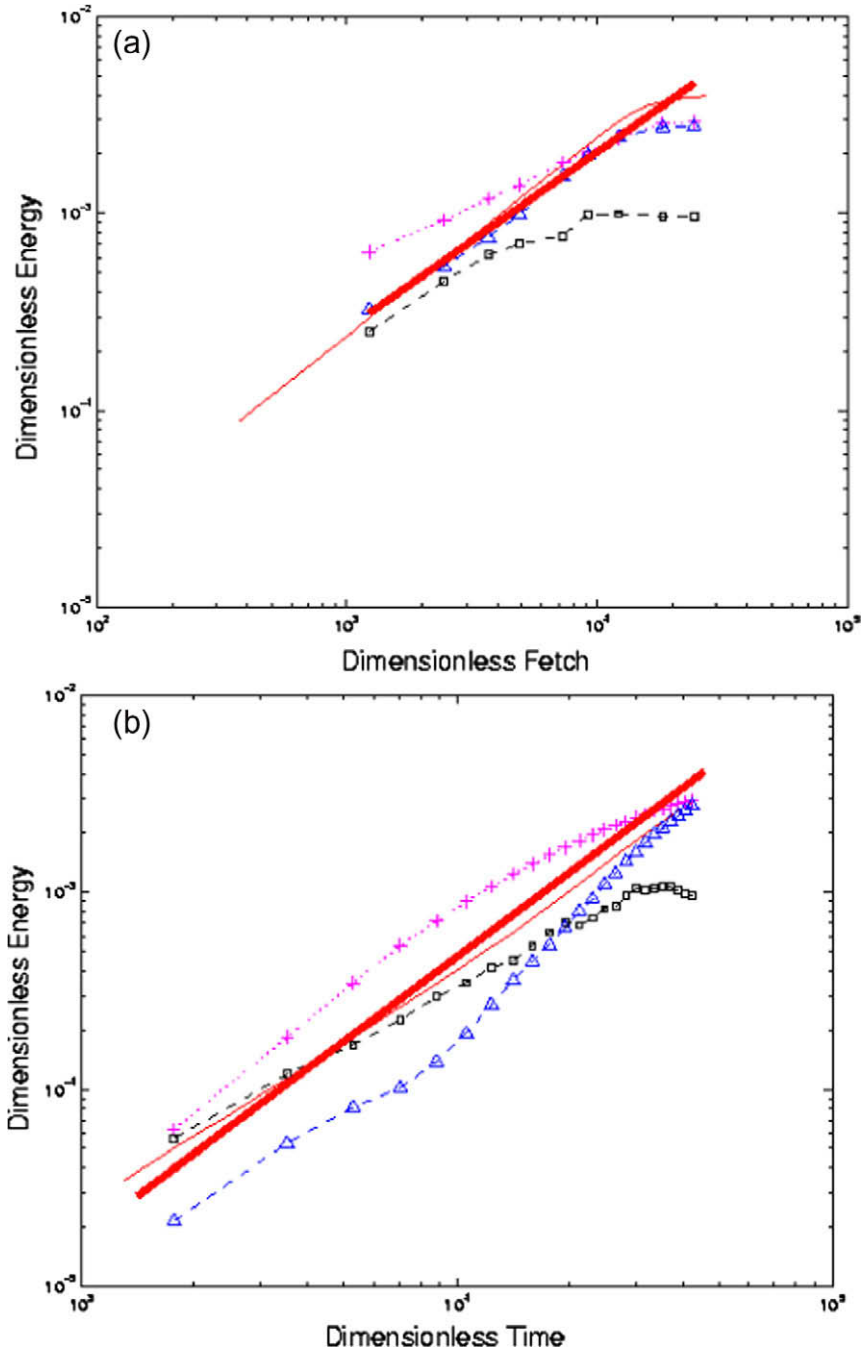

Fig. 9. Energy –growth relations for dimensionless total energy as a function of (a) dimensionless fetch and (b) dimensionless time, comparing derived growth relations from JONSWAP observations (—), Holthuijsen (2007) (—) and results from WW3-AvDI (□– – –), WW3-WRT (Δ – Δ –) and WW3-DIA (+ · · · ·).

scaled as E_g^2/U_{10}^4 where g is gravitational acceleration, and U_{10} is the reference 10 m wind speed. Dimensionless time is T_g/U_{10}, and dimensionless fetch is $\times g/U_{10}^2$. These results correspond to SWAMP case 2 in Hasselmann et al. (1985), assuming an idealized deep ocean with dimensions $10^3 \times 10^3$ km and a constant uniform wind 20 ms^{-1} blowing orthogonal to the coast. For comparison, we include energy-growth JONSWAP relations from Hasselmann et al. (1985), and more recent versions of these relations from Holthuijsen (2007). Results shown in Fig. 9a and b suggest that WW3-AvDI is able to provide energy-growth relations that are competitive to those of WW3-DIA and WW3-WRT. Future research will focus on re-parameterization and tuning of S_{in} and S_{ds} to improve comparisons with observed data.

4.2. Hurricane Juan

4.2.1. Storm description

A detailed description of hurricane Juan is given by Fogarty et al. (2006) and the Canadian Hurricane Center website (http://projects.novaweather.net/work.html). Juan reached hurricane strength on 26 September near Bermuda, and moved northwestward, as a subtropical ridge to the northward, attaining maximum winds of 90 knots at 1800 UTC on 27 September, as it moved towards Nova Scotia with increasing propagation speed. By 1800 UTC on 28 September, Juan was north of the Gulf Stream, and its intensity began to weaken due to the cooler continental shelf waters. Because of its accelerating translational speed, Juan quickly passed over these cooler waters and made landfall near Halifax (0300 UTC on 29), with sustained winds of 85 knots. A feature of Juan's development is the phenomenal acceleration of its translation speed, increasing from 2.28 ms^{-1} at 1200 UTC on 27 September to 20 ms^{-1} at 1200 UTC on 29 September.

4.2.2. Model set-up

The computational domain was chosen to accommodate the hurricane's path, swell and propagation characteristics, in order to optimally simulate the hurricane-generated wave energy. We used a 15′-resolution domain for the region extending from 40°W to 75°W and from 20°N to 65°N, as shown in Fig. 10.

4.2.3. Wind fields

Xu et al. (2007) discuss the need for high-quality winds in order to avoid biases in wave simulations. Wind errors, particularly in highly complex hurricane cases, can obscure wave model shortcomings. Because of Juan's small spatial structure, and category 2 intensity, operational forecast winds, for example COAMPS winds (Coupled Ocean Atmosphere Prediction System) from FNMOC (Fleet Numerical Meteorological and Oceanographic Center), tend to underestimate the central core storm winds, and overestimate the winds in the outer storm region, away from Juan's center. Moreover, the large time intervals between successive wind maps (6 h for FNMOC winds) and the WW3 wind interpolation algorithm can generate more distortions in the wind fields and the hurricane position (Tolman and Alves, 2005). This distortion is particularly notable for rapidly moving storms. Thus, Xu et al. (2007) used observed wind data and an interpolation methodology to construct relatively high-quality empirical wind fields, employing a rectangular hurricane-centered computation domain (11.2° × 7.2°) along Juan's trajectory. Following Moon et al. (2003), this methodology uses 'best track' data from NHC (USA National Hurricane Center) for the period from 0300 UTC on 27 Sept. to 0900 UTC on 29 Sept. These winds are used in all the wave simulations in this study.

4.2.4. Observed wind and wave data

Observed *in situ* wind and wave data are available from Canadian Meteorological Service of Canada (MSC) buoys 44142 and 44137 located in water depths of 1300 and 4500 m, off Nova Scotia, and from a directional waverider (DWR) near Lunenburg Bay, Nova Scotia in 29 m (Fig. 10). These instruments were located on Juan's storm track (44142); on the right of the track and beyond the peak wind radius (44137); and on the left side near the peak wind radius (DWR). Fig. 11 verifies that parameterized winds constructed from Xu et al.'s (2007) methodology compare relatively well to observed wind speed and directional data at buoys 44137 and 44142.

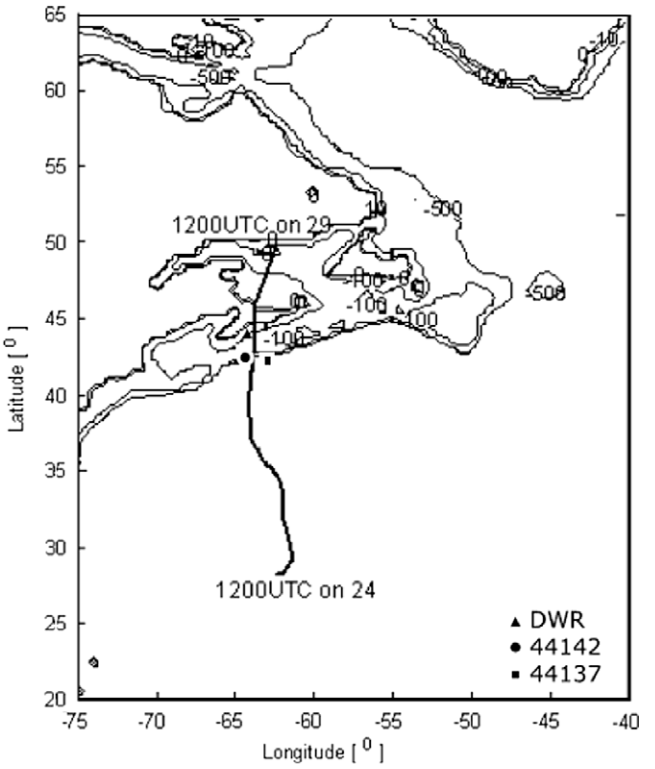

Fig. 10. WW3 grid domain and storm track of hurricane Juan. Observations are at open ocean buoys 44142 (64.02°W, 42.5°N) and 44137 (62.0°W, 42.26°N), respectively, and at the DWR (64.18°W, 44.24°N).

Winds at buoy 44137 reached 21.4 ms^{-1} and significant wave heights (Hs) reached 6.9 m, although lagged behind the winds. By comparison, buoy 44142 on Juan's track recorded winds up to 28.1 ms^{-1} and Hs values that reached 12.1 m. This implies that winds and waves at buoys 44142 and 44137 are quite different, reflecting different locations with respect to the storm and different wave physics related to the storm's passage. Although exposed to the open ocean, the DWR was relatively near the coast, and about 25 km to the left of Juan's track. It recorded Hs values up to 9.2 m and peak wave directions of 183°.

4.2.5. Wave height and period simulations

Estimates of Hs and peak period (T_p) values from WW3-AvDI and WW3-DIA are compared with observations in Figs. 12 and 13. These results suggest that both WW3-AvDI and WW3-DIA are capable of simulating waves during hurricane Juan reasonably well. Results from both models are comparable to observed Hs and T_p values. These results are in conjunction with assumed parameterizations for S_{in} and S_{ds}; different functional forms for S_{in} and S_{ds} would give somewhat different results.

The comparisons of model and observed data (Figs. 12 - Fig. 13) show some biases. At buoy 44137, as seas begin to build to Juan's maximum intensity (before about 1800 UTC on 28 September), simulated Hs estimates agree relatively well with observations from both WW3-AvDI and WW3-DIA, while simulated T_p values

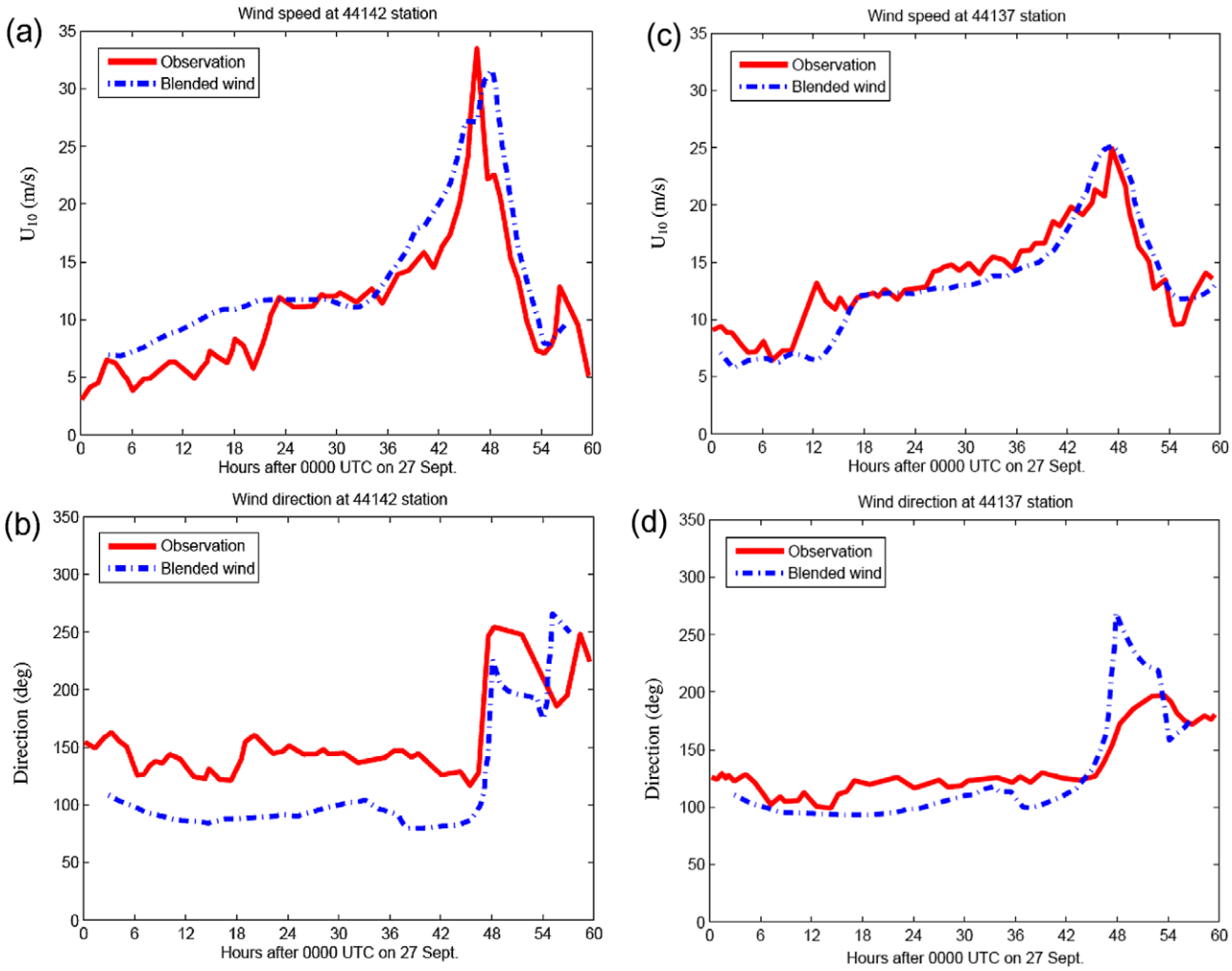

Fig. 11. Comparison between blended winds and observations (from Xu et al., 2007) at buoy 44137, for (a) wind speed and (b) wind direction. Comparison between blended winds and observations at buoy 44142 for (c) wind speed and (d) wind direction.

are biased low. During the storm's maximum intensity (after 1800 UTC on 28 September), simulated T_p values are in reasonable agreement with observations. However, WW3-DIA overestimated the peak Hs by about 3 m, whereas WW3-AvDI overestimated the peak Hs by about 1.5 m. At buoy 44142, the observed peak Hs is underestimated by WW3-AvDI by about 2.5 m, whereas WW3-DIA suggests an underestimate by about 2 m. Xu et al. (2007) suggest that overestimates in the modeled sea surface roughness for high winds, as well as strong swell and currents may be contributing factors. By comparison, at the DWR, both models underestimate the maximum Hs by about 2.5 m, during the storm's peak intensity.

4.2.6. One-dimensional wave spectra

The simulated 1D spectra from WW3-AvDI and WW3-DIA exhibit notable differences from one another and from the observed data. Fig. 14a–c compare the simulated 1D spectra with observations at buoys 44137 and 44142 and the DWR at the storm's peak intensity, when wind-generated wave conditions are dominant. In terms of spectral maxima, both WW3-AvDI and WW3-DIA give spectral peaks that overestimate the observed peak at buoy 44137 (Fig. 14a), whereas at buoy 44142, WW3-DIA overestimates the observed peak and WW3-AvDI gives an underestimate (Fig. 14b). At the DWR (Fig. 14c), the maximum from WW3-DIA appears similar to the observed maximum, whereas WW3-AvDI gives an underestimate.

At buoy 44137, the 1D spectral distributions of both WW3-DIA and WW3-AvDI suggest 1D energy levels that exceed the observed data almost throughout the entire spectrum, including the spectral forward face, rear face, and the equilibrium range. Thus, the overall integrated effect is that the maxima in the Hs time series resulting from WW3-DIA and WW3-AvDI (Fig. 12a) exceed the observed Hs. The observed 1D spectral data exhibits several secondary peaks in the rear face and equilibrium range of the spectrum. These secondary peaks are not captured by the WW3-AvDI simulation, whereas WW3-DIA exhibits a secondary peak at about 0.1 Hz. These results suggest that the formulations for S_{in} and S_{ds} are not able to notably change AvDI's tendency to provide relatively smooth results, and do not appreciably smooth DIA's tendency to create multi-mode spectra, shown in Figs. 4–8.

At buoy 44142, both WW3-DIA and WW3-AvDI underestimate the 1D energy spectra on the forward face of the spectrum. Although WW3-AvDI underestimates the energy in the spectral peak region, it attains a good overall simulation for the rear face and equilibrium range of the spectrum. Thus integrating the entire spectrum, WW3-AvDI gives an underestimate for Hs at the storm's peak intensity shown in Fig. 12b. By comparison, although WW3-DIA overestimates the 1D peak spectral energy and approximately simulates the overall energy on the rear face and equilibrium range

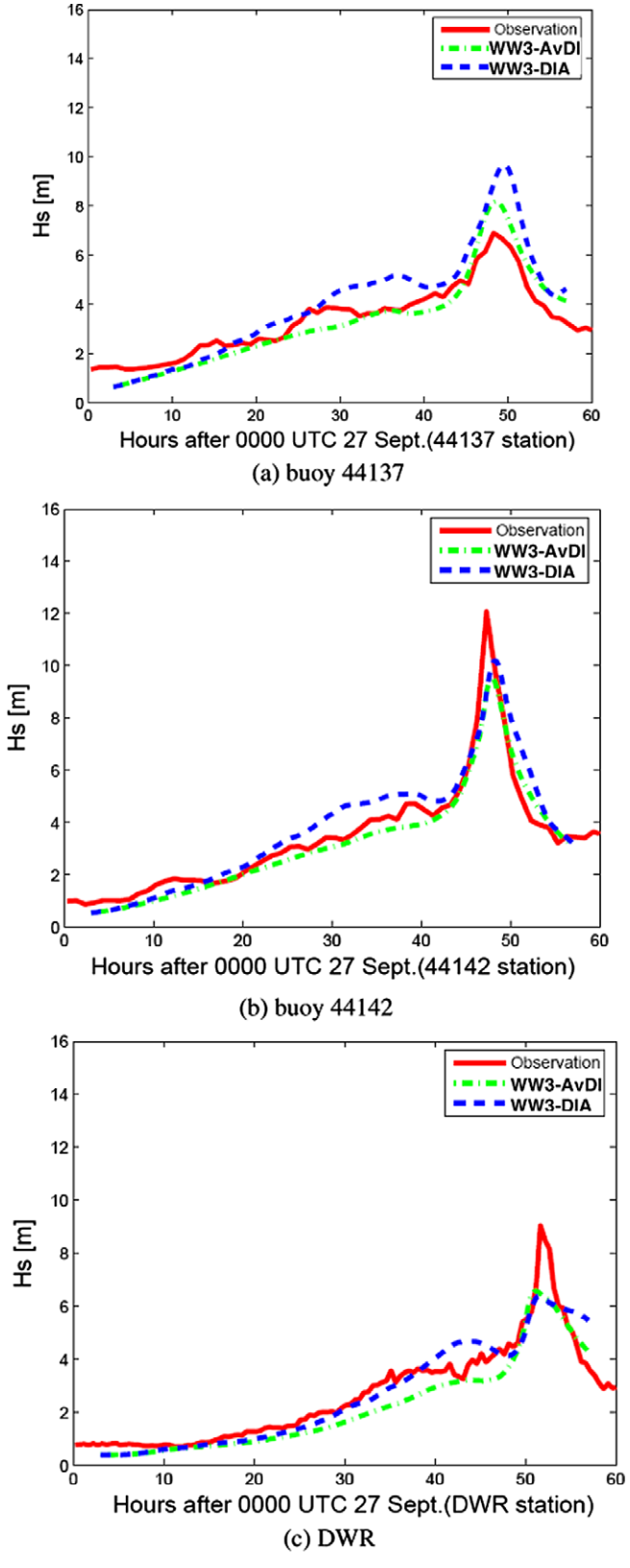

Fig. 12. Comparisons of observed and simulated Hs at different buoy locations.

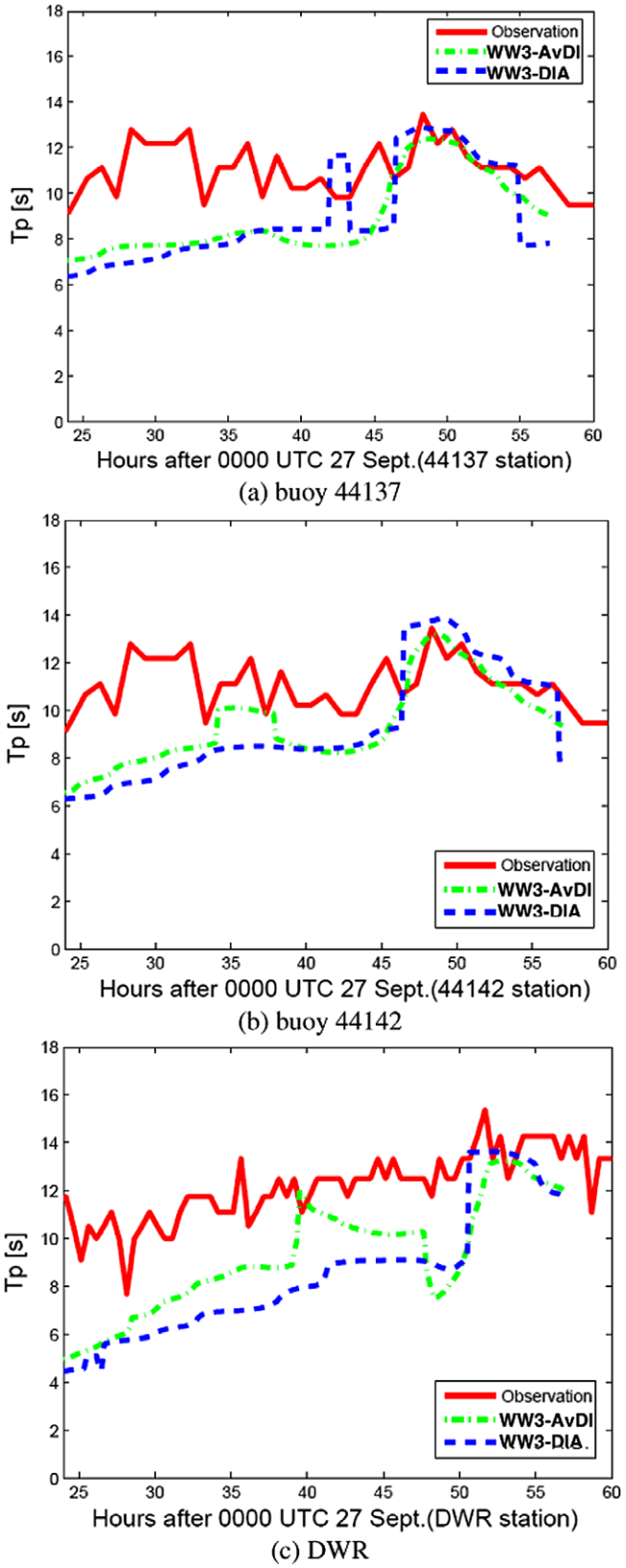

Fig. 13. Comparisons of observed and simulated T_p at different locations.

of the spectrum, it also underestimates the storm's maximum Hs (Fig. 12b), but not to the extent of the WW3-AvDI results.

As at buoy 44137, the observed 1D spectral data at buoy 44142 exhibit secondary peaks in the rear face and equilibrium range of the spectrum, possibly representing sea and swell interactions as the storm passes this location. As in Fig. 14a, these secondary peaks are not captured by the WW3-AvDI simulation, which is quite smooth on the spectral rear face and equilibrium range. These results suggest that the S_{in} and S_{ds} formulations do not

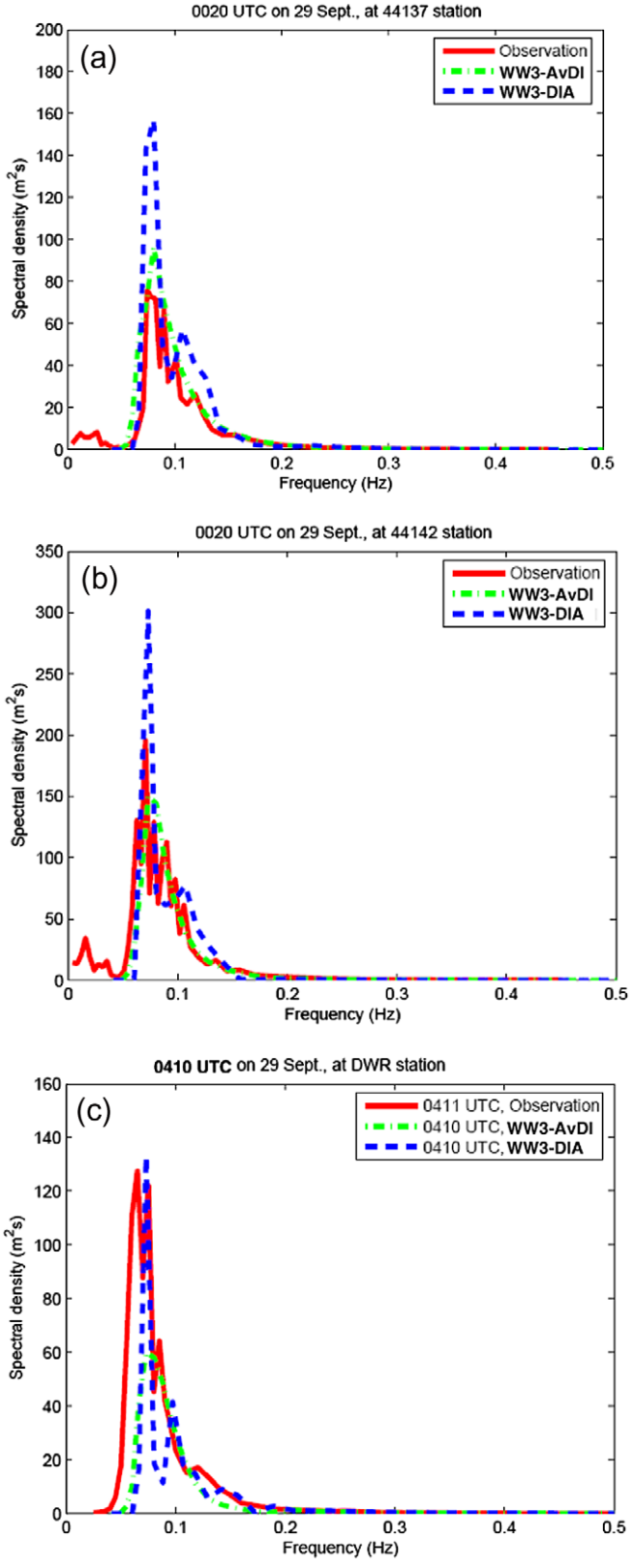

Fig. 14. Comparison of one-dimensional spectra from WW3-AvDI and WW3-DIA to observations at Juan's maximum intensity at 0020 UTC on 29 September at buoys (a) 44137 and (b) 44142. Comparison of one-dimensional spectra from WW3-AvDI and WW3-DIA to observed data at Juan's maximum intensity at the DWR.

notably change AvDI's tendency to give relatively smooth results, nor do they smooth DIA's tendency to create multi-mode spectra (Figs. 4–8).

At the DWR, both WW3-DIA and WW3-AvDI seriously underestimate the spectral energy on the forward face, and suggest spectral peaks (f_p) that are higher than observed. WW3-DIA attains a peak spectral energy that approximates the observed data but underestimates the energy of the rear face. By comparison, WW3-AvDI underestimates the spectral maximum, but attains a reasonable simulation of the equilibrium range energy. Both models result in approximately the same maximum Hs values (Fig. 14c) which underestimate the observed maximum Hs. As in Fig. 14a and b, we see again that the observed DWR spectrum exhibits secondary peaks in the rear face and equilibrium range, which are not captured by the WW3-AvDI simulation. By comparison the WW3-DIA results suggest two different secondary spectral peaks in the rear face and equilibrium range of the spectrum, and very high peakedness.

4.2.7. Two-dimensional wave spectra

Two-dimensional (2D) results of simulated wave spectra and the observed DWR data are given in Fig. 15. These measurements are not available from buoys 44137 or 44142. The 2D spectra measured by the DWR are derived using the maximum entropy method (MEM) as provided by Datawell BV Oceanographic Instruments http://download.datawell.nl/documentation/datawell_brochure_waves21_2006-03-10.pdf.

Fig. 15a–c coincide with the dominance of the wind-generated waves (0411 UTC on 29 September). After this time, swell becomes more evident. At this time, the observed spectral peak is relatively narrow in the directional range and broadens in the rear face and equilibrium range of the spectrum (Fig. 15a). The spectral maximum is 13.09 m^2 /Hz/rad. Directional shearing is evident at high frequencies in the equilibrium range due to veering wind directions, as the hurricane moves past the buoy.

The simulated spectra generated by WW3-DIA and WW3-AvDI are shown in Fig. 15b and c. Both simulations underestimate the spectral energy on the forward face of the spectrum shown in Fig. 15a. The simulated spectrum from WW3-DIA (Fig. 15b) exhibits a relatively narrow spectral peak region and suggests directional shearing in the equilibrium range. The WW3-DIA spectral peak (5.71 m^2/Hz/rad) underestimates the observed spectral peak and the simulated spectrum lacks directional broadening in the rear face and equilibrium range, which is suggested in the observed data. The observed secondary peaks at about 0.09 and 0.12 Hz in Fig. 14c are represented in the two-dimensional spectrum in Fig. 15a, but are not as evident in WW3-DIA results (Fig. 15b). Narrowness in WW3-DIA's 2D spectrum is notable and compares well to observed data in the spectral peak and rear face regions of the spectrum. The secondary peak suggested by WW3-DIA at about 0.1 Hz in the 1D spectrum of Fig. 14c is also evident in Fig. 15b, but is not apparent in the observed spectrum.

The simulated results from WW3-AvDI (Fig. 15c) suggest directional shearing and directional broadening in the rear face and equilibrium range, which is similar to the observed data (Fig. 15a). The 2D spectrum from WW3-AvDI is smoother than the observed data. Although WW3-AvDI underestimates the maximum spectral peak (2.55 m^2/Hz/rad), the breadth of its simulated spectrum in the equilibrium range gives Hs estimates that approximate those of the WW3-DIA simulation (Fig. 12c). However, WW3-AvDI results do not suggest pronounced secondary spectral peaks, present in observed data (Figs. 14c and 15a).

5. Conclusions

We have presented a new formulation (denoted AvDI) for the quadruplet wave–wave interactions (S_{nl}), which are central to simulation of ocean surface waves. The new formulation is relatively efficient and accurate, and has potential for application within wave forecast models. In overview, the AvDI approach is built on

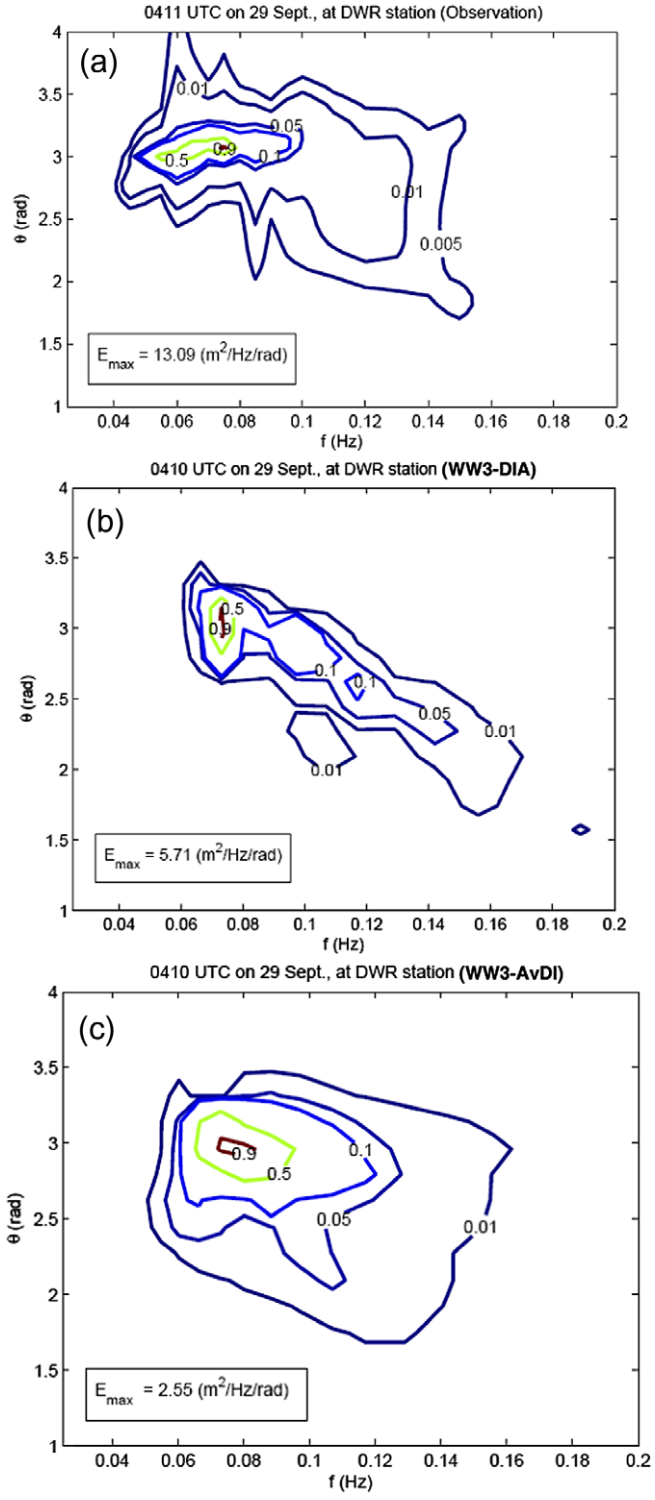

Fig. 15. Two-dimensional spectra at the DWR location, at the time of maximal wave energy, showing (a) DWR observations, (b) WW3-DIA simulation, and (c) WW3-AvDI simulation. Contours indicate fraction of E_{max} with contours values of: 0.005, 0.01, 0.05, 0.10, 0.50 and 0.9. Direction is given by the nautical convention.

the scaling similarities used by the WRT method. Here, WRT denotes the Webb–Resio–Tracy algorithm of Webb (1978), Tracy and Resio (1982) and Resio and Perrie (1991). The AvDI approach selects a set of coordinates $(\mathbf{k}_1, \mathbf{k}_{3_d})$ giving the dominant transfer, in terms of wavenumber and spreading angles. A multiplicative scaling factor F_d is then used to approximate the transfer over the entire 2-dimensional spectrum, based on the transfer at $(\mathbf{k}_1, \mathbf{k}_{3_d})$. As this is representative approach, calibration of the dominant transfer at $(\mathbf{k}_1, \mathbf{k}_{3_d})$ is important. Thus the AvDI approximation can represent contributions from the full integral based on a sample from the entire integral that is shown to have a consistent relationship to the full integral (Figs. 4–8). This is the AvDI approach. The full integral, on the average, is expected to be a factor of F_d larger than the largest dominant transfer at $(\mathbf{k}_1, \mathbf{k}_{3_d})$, at specific spreading angles. In this paper, the AvDI methodology used $2\pi^{-1}\cos^{2n}\theta$ as the assumed spreading distribution to train the method. Although further training of the model could include bimodal distributions, as suggested by recent observations by Long and Resio (2007), these effects are expected to be secondary.

We demonstrated the AvDI method for several cases of JONSWAP spectra, and implemented it within a modern operational wave forecast model WW3, replacing the DIA (Discrete Interaction Approximation) which is the standard algorithm used in modern operational wave forecast models. The newly modified WW3 (denoted WW3-AvDI) was tested for a real storm case. We simulated hurricane Juan, which made landfall in Nova Scotia in September 2003 as a category 2 hurricane. Comparisons include the AvDI, DIA and WRT formulations for the nonlinear transfer (S_{nl}).

Using JONSWAP test spectra we show that AvDI is more accurate than DIA, with respect to WRT. Comparisons included 1D and 2D distributions of the nonlinear transfer. The extent of the agreement between AvDI and WRT is notable. Comparisons with real data from observations collected during hurricane Juan are less unequivocal. We show that WW3-AvDI is competitive with WW3-DIA in estimating significant wave height Hs and peak periods T_p values. These results are in conjunction with the assumed standard S_{in} and S_{ds} parameterizations. The 1D and 2D spectra observed at hurricane Juan's peak intensity display secondary spectral peaks, possibly representing the interactions of swell and sea. While WW3-DIA suggests some indication of secondary spectral peaks, it does not give an accurate simulation of them, whereas WW3-AvDI produces relative smooth spectra with no notable secondary peaks, suggesting that the assumed S_{in} and S_{ds} formulations do not actively dominate AvDI's tendency to provide rather smooth spectra.

We show that the new AvDI formulation is sufficiently efficient that it is a potential candidate for operational wave forecast model tasks. For the particular grid that was considered in this study, the estimated run time is about 135 times faster than WRT, and 36 times slower than DIA. Much less computational memory is required, compared to WRT, because fewer basic grid points in the wave–wave interaction geometry are needed. Moreover, AvDI results compare relatively well with WRT results, in both 1D and 2D tests. As a prototype, AvDI can be used for practical wave simulations and forecasts. However, before this can be done, it is important to extend the AvDI calibrations in conjunction with changes in the wind input S_{in} and dissipation S_{ds} source terms. Additional research will focus on S_{in} and S_{ds} formulations.

Acknowledgements

The authors are grateful to two anonymous reviewers whose comments helped to greatly improve the manuscript. We also want to thank Dr. Don Resio for comments and very helpful suggestions, and Prof. Fumin Xu for wind fields for hurricane Juan. We thank the Natural Sciences and Engineering Research Council (NSERC) of Canada, the Canada Foundation for Climate and Atmospherics Sciences, the Panel of Energy Research and Development.

Appendix A

A full discussion of the numerical methods used in Section 2 is given by Krommer and Ueberhuber (1994) and Ueberhuber (1997),

and also described at http://mathworld.wolfram.com. We applied the closed Newton–Cotes formula, also known as the trapezoidal rule, and implemented the 10-point approximation formula from Ueberhuber (1997) after some numerical experimentation to optimize the calculation. Increased numbers of points in the approximation formula result in a minor reduction in errors, but require more time for the calculation. The approximation has relatively small error that is not changing appreciably and the calculation time is acceptable for available computer resources. The 10-point approximation formula is

$$\int_{x1}^{x10} f(x)\mathrm{d}x = \frac{9}{89,600}h[2857(f_1+f_{10}) + 15,741(f_2+f_9) + 1080(f_3+f_8) + 19,344(f_4+f_7) + 5778(f_5+f_6)] - \frac{173}{14620}h^{11}f^{(10)}(\xi) \tag{A1}$$

where the last term represents the magnitude of the error and $x_1 \leqslant \xi \leqslant x_2$. Therefore, as an example of the integration for a half plane only, we can express the integral along the resonance loci as

$$\int_{1}^{locus/2} f(s)\mathrm{d}s = \frac{9}{89,600}\Delta s[2857(f_{s1}+f_{s10}) + 15,741(f_{s2}+f_{s9}) + 1080(f_{s3}+f_{s8}) + 19,344(f_{s4}+f_{s7}) + 5778(f_{s5}+f_{s6})] - \frac{173}{14,620}\Delta s^{11}f^{(10)}(\xi). \tag{A2}$$

The complete expression is similar for terms f_{s11} to f_{s20}.

References

Fogarty, C.T., Greatbatch, R.J., Ritchie, H., 2006. The role of anomalously warm sea surface temperatures on the intensity of Hurricane Juan (2003) during its approach to Nova Scotia. Mon. Wea. Rev. 134, 1484–1504.

Hashimoto, N., Kawaguchi, K., 2001. Extension and modification of Discrete Interaction Approximation (DIA) for computing nonlinear energy transfer of gravity wave spectrum. In: Ocean Wave Measurement and Analysis. ASCE, pp. 530–539.

Hasselmann, K., 1962. On the nonlinear energy transfer in a gravity wave spectrum, Part 1. J. Fluid Mech. 12, 481–500.

Hasselmann, S., Hasselmann, K., 1981. A symmetrical method of computing the nonlinear transfer in a gravity wave spectrum. Max Planck Inst. Tech Report, Hamburg, p. 174.

Hasselmann, S., Hasselmann, K., 1985. Computations and parametrizations of the nonlinear energy transfer in a gravity wave spectrum, Part I, A new method for efficient computations of the exact nonlinear transfer integral. J. Phys. Oceanogr. 15, 1369–1377.

Hasselmann, K., Barnett, T.P., Bouws, E., Carlson, H., Cartwright, D.E., Enke, K., Ewing, J.A., Gienapp, H., Hasselmann, D.E., Kruseman, P., Meerburg, A., Muller, P., Olbers, D.J., Richter, K., Sell, W., Walden, H., 1973. Measurements of wind-wave growth and swell decay during the Joint North Sea Wave Project (JONSWAP). Deutsche Hydrograph. Zeit. Ergänzungsheft, Reihe A8 (12), 95.

Hasselmann, S., Hasselmann, K., Allender, J.H., Barnett, T.P., 1985. Computations and parameterizations of the nonlinear energy transfer in a gravity-wave spectrum. Part II: parameterizations of the nonlinear energy transfer for application in wave models. J. Phys. Oceanogr. 13, 1378–1391.

Holthuijsen, L.H., 2007. Waves in Oceanic and Coastal Waters. Cambridge Univ. Press. p. 387.

Komen, G.J., Cavaleri, L., Donelan, M., Hasselmann, K., Hasselmann, S., Janssen, P.A.E.M., 1994. Dynamics and Modelling of Ocean Waves. Cambridge University Press, England, UK. p. 532 + xxi.

Krasnopolsky, V.M., Chalikov, D.V., Tolman, H.L., 2002. A neural network techique to improve computational efficiency of numerical oceanic models. Ocean Model. 4, 363–383.

Krommer, A.R., Ueberhuber, C.W., 1994. Numerical Integration on Advanced Computer Systems. Springer-Verlag, Berlin. p. 341.

Lin, R.Q., Perrie, W., 1999. Wave–wave interactions in finite depth water. J. Geophys. Res. 104 (no. c5), 11193–11213.

Long, C.E., Resio, D.T., 2007. Wind wave spectral observations in Currituck Sound, North Carolina. J. Geophys. Res. 112, C05001. doi:10.1029/2006JC003835.

Moon, I.J., Ginis, I., Hara, T., Tolman, H.L., Wright, C.W., Walsh, E.J., 2003. Numerical simulation of sea surface directional wave spectra under hurricane wind forcing. J. Phys. Oceanogr. 33, 1680–1705.

Padilla-Hernández, R., Perrie, W., Toulany, B., Smith, P.C., 2007. Modelling of two northwest Atlantic storms with third generation wave models. Weather & Forecast. 22 (No. 6), 1229–1242.

Perrie, W., Resio, D.T., 2009. A two-scale approximation for efficient representation of nonlinear energy transfers in a wind wave spectrum, Part 2: application to observed wave spectra. J. Phys. Oceanogr. 39, 2451–2476.

Resio, D.T., Perrie, W., 1991. A numerical study of nonlinear energy fluxes due to wave–wave interactions. Part 1. Methodology and basic results. J. Fluid Mech. 223, 609–629.

Resio, D.T., Perrie, W., 2008. A two-scale approximation for efficient representation of nonlinear energy transfers in a wind wave spectrum, part 1: theoretical development. J. Phys. Oceanogr. 38, 2801–2816.

Susilo, A., Perrie, W., 2007. A dominant transfer approximation for the nonlinear wave–wave interactions in wind wave spectra. Int. J. Appl. Math. Eng. Sci. (IJAMES) 1 (No. 1), 53–68.

Susilo, A., Perrie, W., Rahman, M., 2007. Applied dominant transfer and fuzzy logic for nonlinear wave–wave interactions. Int. J. Appl. Math. Eng. Sci. (IJAMES) 1 (No. 1), 11–25.

Tolman, H.L., 1999. User manual and system documentation of WAVEWATCH III version 1.18. NOAA/NWS/NCEP/OMB Technical Note 166, p. 110. Available from: <http://polar.ncep.noaa.gov/waves>.

Tolman, H.L., 2002. User manual and system documentation of WAVEWATCH III version 2.22. Technical Note. Available from: <http://polar.ncep.noaa.gov/waves>.

Tolman, H.L., 2004. Inverse modeling of discrete interaction approximations for nonlinear interactions in wind waves. Ocean Model. 6, 405–422.

Tolman, H.L., Alves, J.H.G.M., 2005. Numerical modeling of wind waves generated by tropical cyclones using moving grid. Ocean Model. 9, 305–323.

Tolman, H.L., Chalikov, D.V., 1996. Source terms in a third-generation wind-wave model. J. Phys. Oceanogr. 26, 2497–2518.

Tolman, H.L., Krasnopolsky, V.M., 2004. Nonlinear interactions in practical wind wave models. In: Proceedings of 8th International Workshop on Wave Hindcasting and Forecasting, Turtle Bay, Hawaii, E.1, CD-ROM.

Tolman, H.L., Krasnopolsky, V.M., Chalikov, D., 2005. Neural network approximations for nonlinear interactions in wind wave spectra: direct mapping for wind seas in deep water. Ocean Model. 8, 253–278.

Tracy, B.A., Resio, D.T., 1982. Theory and calculation of the nonlinear energy transfer between sea waves in deep water. WIS Report 11, p. 47.

Ueberhuber, C.W., 1997. Numerical Computation 2: Methods, Software, and Analysis. Springer, Berlin. p. 496.

Van Vledder, G.Ph., 2001. Extension of the discrete interaction approximation for computing nonlinear quadruplet wave–wave interactions in operational wave models. In: Proc. 4th ASCE Int. Symp. on Ocean Waves, Measurements and Analysis, San Francisco, California, USA, pp. 540–549.

Van Vledder, G.Ph., 2006. The WRT method for the computation of non-linear four-wave interactions in discrete spectral wave models. Coastal Eng. 53, 223–242.

WAMDI Group (13 authors), 1988. The WAM model – a third generation oceans wave prediction model. J. Phys. Oceanogr. 18, 1775–1810.

Webb, D.J., 1978. Non-linear transfers between sea waves. Deep Sea Res. 25, 279–298.

Xu, F., Perrie, W., Toulany, B., Smith, P.C., 2007. Wind-generated waves in hurricane Juan. Ocean Model. 16, 188–205.

Zakharov, V.E., Filonenko, N.N., 1966. The energy spectrum for stochastic oscillation of a fluid's surface. Dokl. Akad. Nauk. 170, 1992–1995.